



OPEN ACCESS

EDITED BY
Sebastian Uhlemann,
Berkeley Lab (DOE), United States

REVIEWED BY
Arkoprovo Biswas,
Banaras Hindu University, India
Sina Saneiyani,
University of Oklahoma, United States

*CORRESPONDENCE
Jakob Gallistl,
jakob.gallistl@tuwien.ac.at

SPECIALTY SECTION
This article was submitted to
Hydrosphere,
a section of the journal
Frontiers in Earth Science

RECEIVED 02 April 2022
ACCEPTED 04 August 2022
PUBLISHED 12 September 2022

CITATION
Gallistl J, Schwindt D, Birgit J, Aigner L,
Peresson M and Flores Orozco A (2022),
Quantification of soil textural and
hydraulic properties in a complex
conductivity imaging framework:
Results from the Wolfsegg slope.
Front. Earth Sci. 10:911611.
doi: 10.3389/feart.2022.911611

COPYRIGHT
© 2022 Gallistl, Schwindt, Birgit, Aigner,
Peresson and Flores Orozco. This is an
open-access article distributed under
the terms of the [Creative Commons
Attribution License \(CC BY\)](https://creativecommons.org/licenses/by/4.0/). The use,
distribution or reproduction in other
forums is permitted, provided the
original author(s) and the copyright
owner(s) are credited and that the
original publication in this journal is
cited, in accordance with accepted
academic practice. No use, distribution
or reproduction is permitted which does
not comply with these terms.

Quantification of soil textural and hydraulic properties in a complex conductivity imaging framework: Results from the Wolfsegg slope

Jakob Gallistl^{1,2*}, Daniel Schwindt³, Jochum Birgit⁴,
Lukas Aigner¹, Mandana Peresson⁴ and Adrián Flores Orozco¹

¹Geophysics Research Division, Department of Geodesy and Geoinformation, TU Wien, Vienna, Austria, ²Section Applied Geophysics, Department of Geophysics, Central Institution for Meteorology and Geodynamics (ZAMG), Vienna, Austria, ³Department of Physical Geography, Institute of Geography, University of Göttingen, Göttingen, Germany, ⁴Department of Geophysics, Geological Survey of Austria, Vienna, Austria

We present an approach that permits to predict hydraulic conductivity from extensive, multi-methodical geophysical data collected on a hillslope affected by landslides in Austria. The objective of the investigation is the spatial characterization of a slope affected by mass movements to derive hydrogeological structures and preferential flow paths. The geophysical data sets presented in this study consists of 24 densely distributed complex conductivity (CC) imaging profiles, collocated to these profiles we also collected 517 transient electromagnetic (TEM) soundings and 10 refraction seismic tomography (RST) profiles. Additionally, we also present well-logging data (namely electrical resistivity, natural gamma logs) collected in five boreholes. Cores recovered during the drilling of the boreholes are used to aid in the interpretation of the geophysical units, while analysis of the sediments was conducted to obtain grain size distributions, cation exchange capacity and mineralogy of the subsurface materials. While all geophysical data was processed initially independently, the final complex conductivity imaging results are based on the incorporation of structural constraints about the electrical units obtained from the TEM soundings. The interpretation of the resolved CC units is then sustained by the RST images and the lithological information from the boreholes. We estimate then the hydraulic conductivity of the subsurface derived from the CC images using a two-step approach. In a first step, we investigated the link between the complex conductivity and the different soil volume fractions of gravel, sand, silt and clay. In a second step, we applied a pedo-transfer function, namely the well-known Rosetta model, that permits to predict the hydraulic conductivity from the estimated grain size volumes. This approach allowed a quantitative interpretation of the geophysical data and thus a 3-dimensional (3D) representation of the grain size distribution and hydraulic conductivity in the investigated slope section. Thereby, we observed well-determined site-specific relationships ($R^2 > 0.7$) from the comparison of the complex resistivity images and grain size analysis. The obtained hydrogeophysical 3D model permits to delineate the geometry of an aquiclude, and, thus, the analysis of preferential water-flow paths. In

particular, we can identify a spatial correlation between the aquiclude interface and morphological features.

KEYWORDS

soil-textural parameters, complex conductivity imaging, hydrogeophysics, induced polarization, transient electromagnetic method, hydraulic conductivity

1 Introduction

Current forecasts assume that the trend towards rising temperatures and precipitation extremes (Dunn et al., 2020) will continue and that the occurrence of droughts (e.g., Cook et al., 2018; Balting et al., 2021) and heavy rainfall (Ban et al., 2015; Papalexioiu and Montanari 2019) can will increase in the next years. Such meteorological changes affect ecosystems (e.g., Weiskopf et al., 2020), land use (Searchinger et al., 2018), water availability (Konapala et al., 2020), but also natural disasters such as floods (Tabari 2020) and mass movements (Alvioli et al., 2018; Lin et al., 2020). In this context, a comprehensive understanding of the hillslope hydrology is of fundamental importance, to predict runoff responses (Blume and Van Meerveld 2015), but also in the understanding of the hydraulic properties of the subsurface triggering landslide processes (Bogaard and Greco 2016). The complex sedimentary structures in hillslopes, as a result of geological disposition and local geomorphodynamics, make prediction of hydrological processes immensely difficult (Sidle et al., 2019). Small-scale variations in sediment characteristics and the associated hydraulic properties affect infiltration, percolation, but also evaporation (Lehmann et al., 2018) as well as water storage (Berg et al., 2017) and affects hydrologic connectivity via surface runoff and subsurface flow. As a consequence, slope architecture may be related to areas of waterlogging, small-scale slumping or subsidence as well as major mass movements. Moreover, Blume and Van Meerveld (2015) conclude, that the subsurface hillslope-stream connectivity is difficult to observe and quantify, and, due to the high variability in hillslope responses, results are hard to extrapolate to other hillslopes. Blume and Van Meerveld (2015) also point out, that multimethod approaches might be useful, as they strengthen the interpretation of individual measurements.

While the description of hillslope properties is often based on point data from core soundings, a spatial approach is needed to deal with the complexity of the slope sediments and the associated hydrology. In recent years, geophysical methods have been increasingly used to spatially characterize the shallow subsurface (Flores Orozco et al., 2018b; Gallistl et al., 2018; Watlet et al., 2018; Huntley et al., 2019; Holmes et al., 2020). Furthermore, approaches to use geophysical imaging as landslide early warning systems, by monitoring short- and long-term moisture dynamics are developed (Whiteley et al., 2021).

Geophysical methods commonly applied in hillslope characterization include the Electrical Resistivity Tomography (ERT) (Perrone et al., 2014), Refraction Seismic Tomography (RST) (Samyn et al., 2012; Uhlemann et al., 2016), and, to a lesser extent Electromagnetic Induction at low induction number (EMI) (Grandjean et al., 2011; Kušnirák et al., 2016), Transient Electromagnetic Sounding (TEM) (Godio and Bottino, 2001; Li et al., 2020) and Induced Polarization Imaging (IP) (Flores Orozco et al., 2018a; Gallistl et al., 2018; Revil et al., 2020).

IP, also referred to as Complex Conductivity Imaging (CCI), is an extension of the ERT method and provides information about the electrical conductivity and capacitive (polarization) properties of the subsurface (Kemna et al., 2012). The IP method was developed for the prospection of metallic mineral ores given the strong IP response in the presence of iron sulphides (Pelton et al., 1978). In recent years, IP has emerged as a promising method for various environmental and hydrogeological applications including the mapping of geochemical active zones (Flores-Orozco et al., 2020; Katona et al., 2021), the monitoring of changes in pore-space geometry accompanying bioremediation processes (Flores Orozco et al., 2011; Flores Orozco et al., 2019) and the assessment of permafrost degradation (Doetsch et al., 2015; Maierhofer et al., 2022), just to name a few. In the context of characterizing hillslopes affected by landslides, IP has revealed promising results (Flores Orozco et al., 2018a; Gallistl et al., 2018; Revil et al., 2020), as numerous laboratory studies reported a sensitivity of the IP method to soil-textural properties of the subsurface (Slater and Glaser, 2003; Tarasov and Titov, 2007; Revil and Florsch, 2010) and, thus, the improved estimation of hydraulic conductivity (Slater et al., 2014; Weller et al., 2015; Weller and Slater, 2019). Since landslides are frequently triggered by heavy precipitation events, resolving changes in textural properties of hillslopes is of great interest as they will determine areas of low hydraulic conductivity (i.e., with a poor drainage) where pore-pressure may accumulate resulting in the triggering of mass movements (Campbell, 1975; Rogers and Selby, 1980). Thus, IP could permit to directly provide estimates of hydraulic conductivity without the need of direct *in-situ* testing not possible in landslides. Unfortunately, the upscaling and transferring of laboratory findings to field-scale measurements has proven difficult so far (Binley et al., 2015).

Over the last few decades, a multitude of pedotransfer functions (PTFs) have been developed that permit the

prediction of soil-hydraulic properties based on commonly available soil information such as soil texture, bulk density and grain size without the need of labor intensive and time-consuming direct measurements (Van Looy et al., 2017; Zhang and Schaap, 2019). Such PTFs provide a viable alternative, if it is possible to define site-specific equations relating the IP effect to soil texture (i.e., the soil volume fractions of sand, silt, clay and gravel) for a quantitative interpretation of IP imaging results in a hydrogeological context. The predictors in PTFs range from relatively simple power model relations (Cosby et al., 1984) to more complex artificial neural networks (Schaap et al., 2001), support vector machines algorithms (Twarakavi et al., 2009), k-nearest neighbor methods (Nemes et al., 2006) and decision/regression trees (Jorda et al., 2015). Rosetta (Schaap et al., 2001), is one of many PTFs that is based on an artificial neural network and uses a hierarchical approach to predict saturated hydraulic conductivity K_s and van Genuchten (VG) water retention parameters (Van Genuchten, 1980). The model input parameters may be given in terms of textural classes, the soil volume fractions of sand, silt and clay (SSC), or as a combination of SSC, bulk density and a referential grain size. As discussed in Zhang and Schaap (2017) the initial version of Rosetta had several deficiencies, which lead to a weighted re-calibration of Rosetta in order to improve the predicted soil-hydraulic properties and reduce uncertainties in their prediction.

The objective of this work is to investigate the spatial prediction of soil-hydraulic properties at the slope scale, based on derivation of soil texture from complex conductivity information and subsequent use of a pedotransfer function (Rosetta). To the best of our knowledge such approach has not been tested for the interpretation of IP imaging data at the field scale. To reduce the uncertainty in IP inversion results, we also present the incorporation of *a priori* information about electrical units obtained from TEM data; additionally, we include refraction seismic tomography as well as soil textural information in boreholes. Using this information, we derive relationships between the complex conductivity and the different soil volume fractions and characterize the main geological units of the study area. To permit a thorough evaluation of our results in a later step, we exclude the information from one borehole. With the obtained prediction functions, we first predict and discuss the soil fractions for a given CCI profile and then use Rosetta to predict K_s . This is followed by a discussion of the implications on water-flow within the slope. We evaluate the performance of our approach based on independent borehole data and discuss our results compared to those obtained by upscaling of laboratory-derived relationships between the IP response and directly measured K_s values.

2 Site description

The study area is located in the municipality of Wolfsegg am Hausruck in Upper Austria, Austria (48°06'34.3"N, 13°40'09.6"E) and comprises an agriculturally used west-east tilted hillside with average slopes of 5–10° and descents with maximum slopes of up to 35°. The area under investigation is limited by a street and settlements to the eastern, and a small stream to the western boundary. The total mean annual precipitation (for the last 23 years) is about 910 mm and the largest precipitation events typically occur between May and August.

The geological frame is given by the Molasse zone that embodies a large Foreland basin from Switzerland in the west across Germany and Austria into the Carpathian Foredeep in the east. The basin fill comprises a section of mainly clastic sediments from the Late Eocene to Late Miocene due to uplift and erosion of the Alpine Orogen (e.g., Rögl, 1997; Hinsch, 2008; Grunert et al., 2010). Stratigraphically, the study area encompasses three main units, which can be listed from top to bottom (Krenmayr and Schnabel, 2006; Rupp et al., 2011) as: the 1) Hausruck, 2) Ampflang, and 3) Ottnang formation, which are partly overlain by quarternary deposits consisting of gravels, sands and silts (see Figure 1A). The predominant unit in the area is the Hausruck formation and comprises fluvial, sandy, and fine to coarse gravels. The Ottnang formation, which constitutes the basal layer of the study area, mostly consists of shallow marine clay silts and marls. Sporadic layers of the Ampflang formation can be found intercalated within the Hausruck and Ottnang units (Figure 1A). The Ampflang formation consists of clay-bearing coal (from limnic and fluvial deposits) with different maturity, which has been exploited sporadically (Rupp et al., 2011). Weathering of the materials of the Hausruck formation resulted in the development of weathered loam, which, in combination with the confining characteristics of the clays in the Ampflang formation, constitute an ideal setting for landslides (Supper et al., 2014).

Baumann et al. (2018) show that landslides are a primary controlling factor for landscape morphology in the Hausruck area. Thus, mass movements have also shaped the slope on which the study area is located. Both, the settlement area on the upper slope, as well as the agricultural areas on the mid- and footslope have been subjected to continuous subsidence over the last 25 years and have called for numerous geotechnical investigations and remediation measures (personal communication with leaseholder of slope). However, even though the slope of the study area was clearly formed by mass movements, anthropogenic overshaping by construction, tillage and drainage works has severely compromised a precise geomorphological site analysis. Based on the analysis of shaded digital terrain models (based on Airborn Laserscanning data at a resolution of 0.5 m, Datasource: Land Oberösterreich - data.ooe.gv.at) in combination with field-based

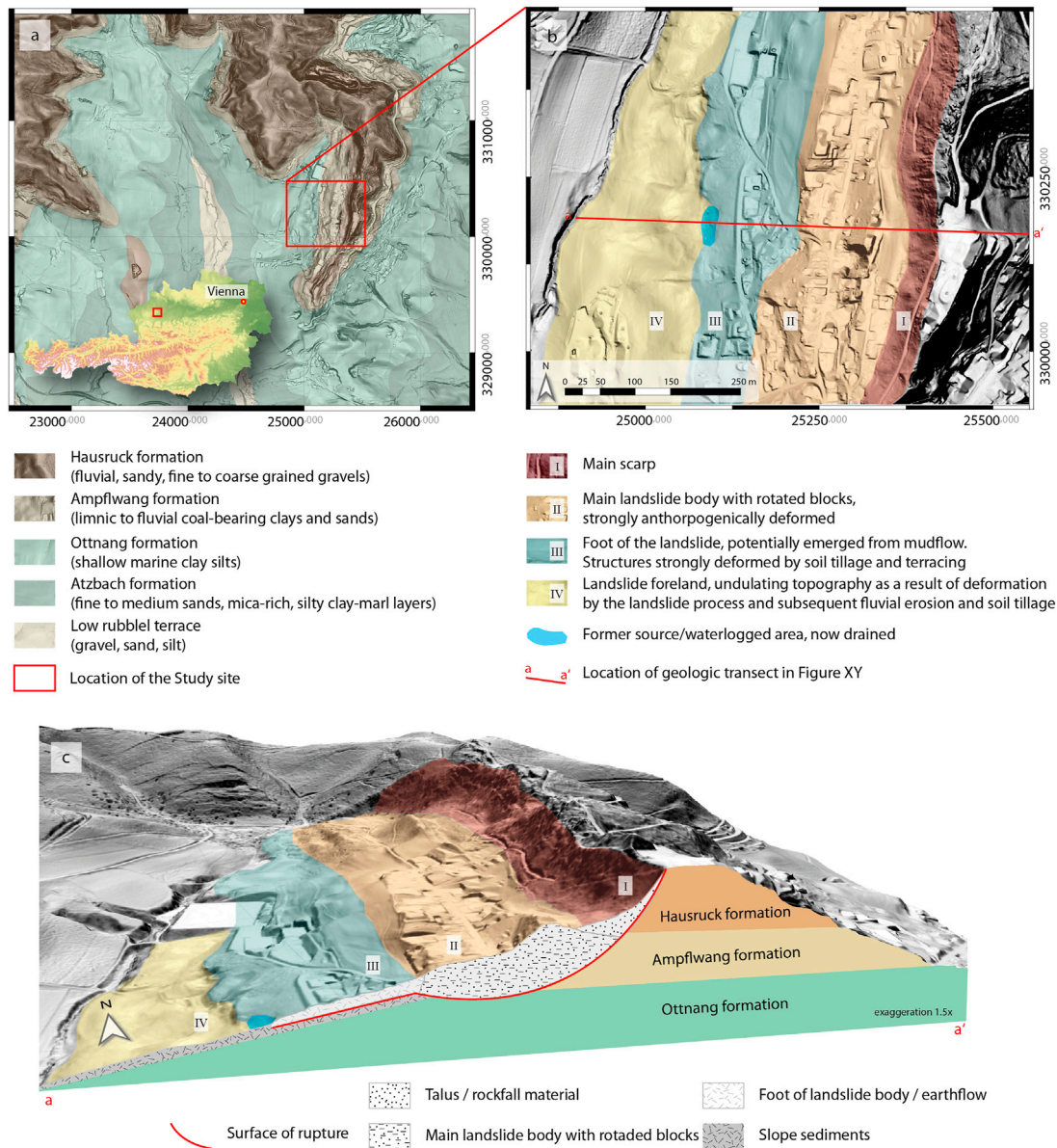
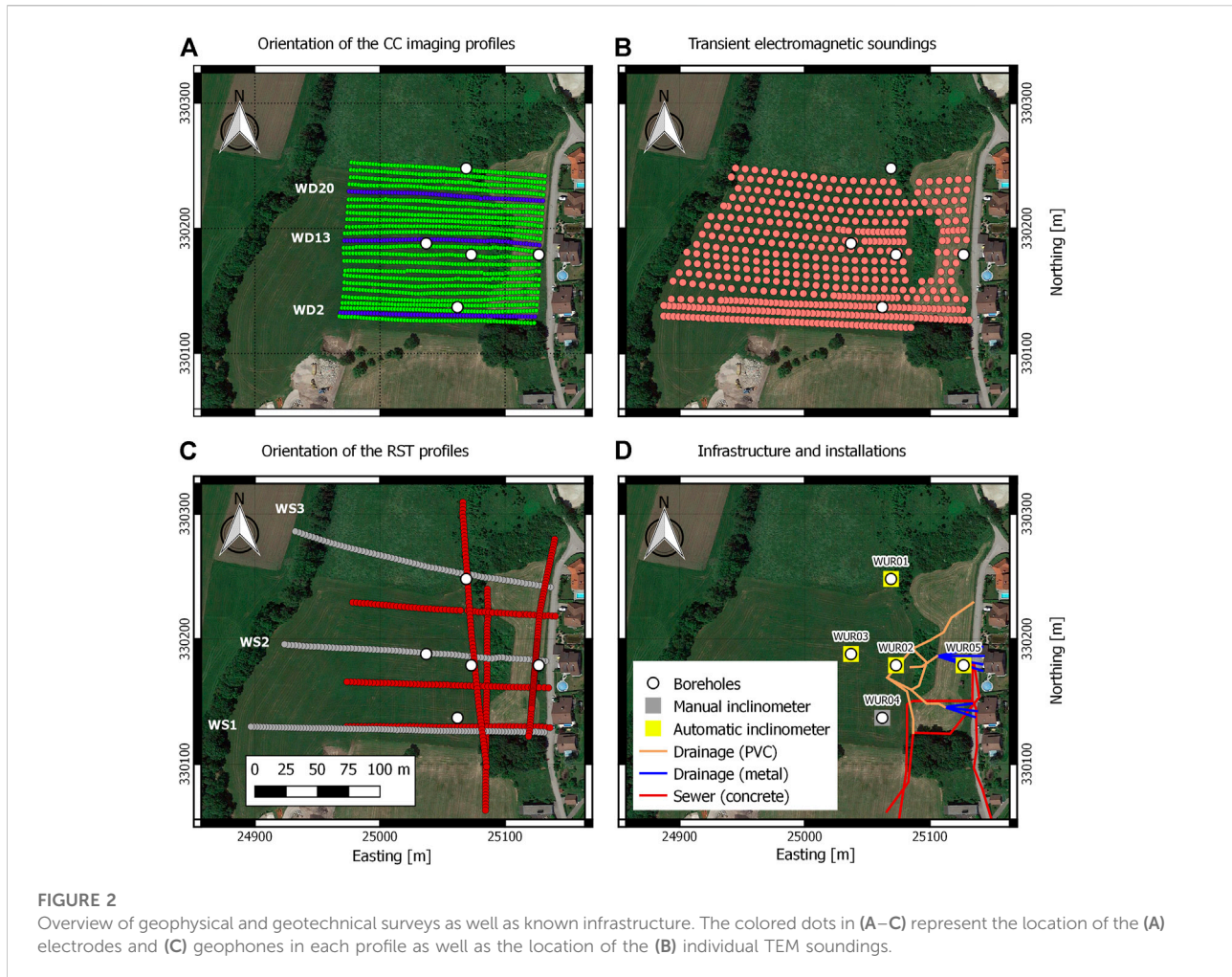


FIGURE 1 Details on the study site Wolfsegg with (A) geological overview of the south-eastern parts of the Hausruck mountain range in Austria (Krenmayr and Schnabel, 2006), (B) shaded digital terrain model with interpreted morphological zones (I-IV) and (C) 3D-scene of the study site with interpreted morphological zones, geology as well as a subsurface model of the slope and landslide body. The reconstruction of the subsurface characteristics is based on the geomorphology of the study site and adopts to the classification of rotational slides by Cruden and Varnes (1996). Elevation data for Figures a–c are based on airborne laserscanning data, resolution 0.5 m, April 2015 (Datasource: Land Oberösterreich—data. ooe.gv.at).

mapping, four morphological zones (cf. Figures 1B,C) can be identified and adopted to the landslide classification according to Cruden and Varnes (1996).

Regarding the four morphological zones, the zone I corresponds to the main scarp, with a height of 30 m and the crown at an elevation of 672 m. A slight flattening at the base of the scarp suggests deposits from rockfall or minor secondary landslide processes. Zone II corresponds to the

main landslide body, which extends for about 250 m horizontal distance and an elevation ranging from 600 to 642 m. Due to construction, zone II exhibits the most severe reshaping. Hence, a too detailed description of its morphology does not seem useful. Nevertheless, two landslide blocks, can be differentiated in this area. A slight dip of the upper block in the direction of the incipient crack indicates a rotational slide (cf. Figure 1C). Zone III, which is



adjacent below, corresponds to the foot of the landslide. Despite the severe anthropogenic overshadowing, tongue-like structures suggests that this area was formed by a mudflow during the landslide process. Zone IV, which adjoins below zone III, is characterized by undulating relief and is interpreted as landslide foreland. The relief formation in this zone is due to deformation of the slope sediments by the surcharge of the landslide masses deposited upslope. Small steps at cropland boundaries indicate prolonged tillage. In the boundary between the landslide toe and zone IV, a morphological hollow form is found that has been interpreted as a former source or waterlogged area (cf. Figures 1B,C). This area has been drained in the last years (cf. Figure 2D). Below the formerly waterlogged area, erosional structures are found in the shaded terrain model that indicate intermittent surface runoff. At 574 m above sea level (a.s.l.), the toeslope is bordered by a small creek in the West of the study site.

In Figure 1C, we present our geomorphologic analysis of the site using the description of rotational slides proposed by

Cruden and Varnes (1996). We assume that the sliding process was initiated on the clay silts of the Ottnag formation. Accordingly, the rotated blocks of the main landslide body in zone II consist of the morphologically hard material of the Hausruck formation (rounded gravels in sandy matrix). The partially tongue-shaped mudflow deposits of zone III are predominantly built up by the materials of the Ampflwang formation (coal-bearing clays and sands). Our conceptual model assumes that a partial mixing of sediments of the Ampflwang formation with materials of the Hausruck formation and slope sediments occurred during the flow process. The shallow subsurface of zone IV, the foreland of the landslide, is built up by old slope sediments. These are most likely composed of a mixture of weathering products of the Ottnag formation intermixed with deposits of the Ampflwang and Hausruck formations. According to our subsurface model, the mudflow on the midslope has overlain old slope sediments, some of which have been incorporated into the mudflow. The uplift pressure of the landslide deposits has caused deformation of the plastic-

reacting slope sediments, resulting in the undulating relief at the footslope in zone IV.

3 Material and methods

3.1 Complex conductivity imaging

The induced polarization (IP)–also known as complex conductivity (CC) or complex resistivity (CR) imaging, is an electrical method that permits to recover information on the subsurface distribution of the resistive (or conductive) and capacitive (or polarization) electrical properties of the subsurface (Ward, 1990; Binley and Kemna, 2005). IP measurements, which can be performed in both time and frequency domain (e.g., Martin et al., 2020), use four electrode configurations—two of them are used for current injection and the other two to record the corresponding voltage. For measurements performed in the frequency domain, a sinusoidal current waveform is used and data collection comprises the measurement of the voltage-to-current ratio and the time delay of the voltage, and therefore, the measurement of a complex-valued electrical impedance (Binley and Kemna, 2005). The collection of such data with different frequencies (10 mHz to 1 kHz), in the so-called spectral IP (SIP), can provide additional information regarding the frequency dependence of electrical properties. IP imaging data sets typically deploy up to hundreds of electrodes for the collection of thousands of four electrode measurements are used in conjunction with inversion algorithms to recover spatially quasi-continuous subsurface models of the electrical properties (Oldenburg and Li, 1994; Kemna, 2000; Binley and Kemna, 2005; Loke et al., 2006).

Inversion results can be given in terms of the complex electrical conductivity $\sigma^*(\omega)$ (where $\omega = 2\pi f$ and f is the excitation frequency), or its inverse, the complex electrical resistivity ρ^* (with $\rho^* = 1/\sigma^*$). The complex conductivity can be expressed by means of its real ($\sigma'(\omega)$), and imaginary ($\sigma''(\omega)$) components, or by its magnitude ($|\sigma^*(\omega)|$) and phase-shift ($\varphi(\omega)$), such as:

$$\sigma^*(\omega) = |\sigma^*(\omega)|e^{i\varphi} = \sigma'(\omega) + i\sigma''(\omega) \quad (1)$$

with $i = \sqrt{-1}$, and further:

$$\varphi = \arctan \frac{\sigma''(\omega)}{\sigma'(\omega)}. \quad (2)$$

The real (or in-phase) component of the complex conductivity represents the conduction (energy loss) properties, while the imaginary (or quadrature) component represents the polarization/capacitive properties (energy storage) of the subsurface. For a detailed review of the IP

method we refer to Ward (1990); Binley and Kemna (2005); Binley and Slater (2020).

The low-frequency (<100 kHz) complex conductivity $\sigma^*(\omega)$ of soils and rocks can be written as a function of a real-valued bulk conductivity, and a complex-valued surface conductivity, such as:

$$\sigma^*(\omega) = \sigma_{bulk} + \sigma'_S(\omega) + i\sigma''_S(\omega). \quad (3)$$

Equation (3) shows that $\sigma^*(\omega)$ consists of a real component that contains contributions from the bulk conductivity σ_{bulk} and a frequency dependent surface conductivity $\sigma'_S(\omega)$, while the imaginary component of $\sigma^*(\omega)$ is only defined by the frequency dependent imaginary surface conductivity $\sigma''_S(\omega)$. The bulk conductivity for an unsaturated sample is given by (Mualem and Friedman, 1991)

$$\sigma_{bulk} = \sigma_f \Phi^m S^n \quad (4)$$

in which Φ is the porosity, S the saturation of the pores, σ_f is the conductivity of the fluid and m, n are empirical coefficients that represent the connectivity between the pores (m) and the saturation degree (n). In case of soils and rocks with clay, organic matter and other minerals with high surface charge and surface area the influences of σ_{bulk} and $\sigma'_S(\omega)$ and particularly the frequency dependence of the latter cannot be neglected. Therefore, the estimation of quantitative petrophysical relationships might be hindered when the surface conductivity is ignored, resulting in poor estimations of hydrogeological parameters, such as hydraulic conductivity or water content. Surface conductivity plays a critical role in presence of grains with a high surface area, and high surface charge (e.g., Waxman and Smits, 1968; Revil et al., 2017). Accordingly, clay minerals are linked to dominating surface conduction mechanisms, and commonly exhibit a high cation exchange capacity (CEC) and electrical conductivity (Revil et al., 2017). Furthermore, Revil et al. (2014) have shown that even for sandstones without clay content the surface conduction might dominate over electrolytic conduction (σ_f). Hence, the knowledge of the contribution of the surface conductivity to the complex conductivity is critical for an adequate interpretation. The imaginary surface conductivity $\sigma''_S(\omega)$ is only related to the imaginary component of the complex conductivity $\sigma''(\omega)$ obtained with IP, such as

$$\sigma''_S(\omega) = \sigma''(\omega) \quad (5)$$

The IP response of soil arises due to polarization processes taking place at the grain-fluid interface, in the so-called electrical double layer (EDL). The polarization of the EDL is caused by the transport and accumulation of electrical charge carriers when subject to an external electrical field during the current injection (Kemna et al., 2012). Electrochemical polarization occurring at the EDL, which includes polarization of the Stern layer (Leroy and Revil, 2009; Revil, 2012) and the diffuse layer (Revil et al., 2017; Bückner et al., 2019a) depends on the electrochemical

TABLE 1 Characteristics of the used electrode configurations, namely, dipole-dipole combining different dipole lengths and multiple-gradient. For the latter, the dipole lengths refer to the size of potential dipoles nested inside the current dipole.

Protocol	Number of quadrupoles	Dipole lengths [m]
Dipole-dipole	2095	2.5, 5, 7.5, 10, 12.5, 15, 17.5, 20, 22.5, 25
Multiple-gradient	1791	2.5, 5, 7.5, 10, 12.5, 22.5, 27.5, 32.5

properties at the grain-fluid interface, i.e., the surface charge of the grain, the specific surface area and salinity of the surrounding electrolyte, as well as the pore-space geometry. For the case of metallic grains, charge carriers inside of the particle also polarize, which further enhances the IP response in the so-called electrode polarization (Revil et al., 2015; Bückler et al., 2018; Bückler et al., 2019b).

3.2 Data collection and processing

To map the complex conductivity response throughout the study area, single frequency (1 Hz) IP imaging data were collected between 12th and 21st June in 2017, along 24 profiles with an orientation west-east deploying in each 64 electrodes with a 2.5 m spacing between the electrodes. 1 Hz as the excitation frequency was chosen as it offered the best compromise between data quality and acquisition time, as higher frequency measurements with reduced acquisition times are highly likely to be distorted by sources of electromagnetic noise (Flores Orozco et al., 2021). We used a DAS-1 instrument (from MultiPhase Technologies, United States) for the collection of the data, always ensuring contact resistances below 5 k Ω resulting in injected currents ranging between 50 and 200 mA. The data were collected using two different electrode configurations: 1) dipole-dipole (DD) combining different skip protocols, where the skip refers to the numbers of electrodes “skipped” in each dipole in order to increase the dipole length (e.g., Flores Orozco et al., 2018a) and 2) multiple-gradient (MG) after Dahlin and Zhou (2006). The characteristics of both configurations can be found in Table 1. Both configurations were designed for an approximate depth of investigation of 30 m and in such a way, that the data cannot be affected by the polarization of the electrodes themselves, i.e., no voltage measurements were performed with electrodes previously used for current injection (Flores Orozco et al., 2018a). To provide a dense distribution of profiles in the area of interest (see Figure 2A), the profile separation was set to 5 m (i.e., twice the electrode spacing). All electrode positions were determined with an RTK-GNSS.

Processing of the data (i.e., outlier removal) is based on the methodology outlined by Gallistl et al. (2018), that originates from the time-domain IP processing scheme proposed by Flores Orozco et al. (2018b). The fundamental idea is that

pseudosections (i.e., a representation of the measured raw data), due to the nature of IP imaging data sets, should reveal spatial consistent patterns, i.e., “smooth” changes in the measured phase-shift ϕ without the occurrence of large discrepancies or abrupt changes. Those measurements with poor spatial consistency can be considered outliers and should be removed prior to inversion. The processing scheme presented in Gallistl et al. (2018) quantifies this spatial consistency in the phase-shift data by grouping measurements collected with the same current dipole, a subsequent computation of a median phase value for measurements in the corresponding group and the computation of a deviation value $\Delta\phi$ for each measurement in the group to the median value. Spatial consistent measurements are then defined as those with a small deviation, whereas measurements related to large deviations are considered outliers and are removed.

Inversions of the imaging data sets were performed with CRTomo (Kemna, 2000), using a robust inversion scheme. Such an approach permits to improve the convergence of the inversion and it is less sensitive to wrong estimates of the data error (LaBrecque and Ward, 1990; Morelli and LaBrecque, 1996; Kemna, 2000). All inversions converged to a root-mean-square error close to 1 and a slightly preferential smoothing in horizontal to vertical direction (10:1) was used. We selected this smoothing factor based on the assumption that deformation of the old slope materials in Zone IV (cf. Figure 1) will follow the uplift pressure of the landslide deposits, resulting in an undulating relief and likely only minor deviations from a horizontal layering. For materials associated to the mudflow in Zone III, intermixing of materials of the Ampflwang, Hausruck and old slope sediments is likely to have occurred. However, we do not believe that the individual layers will deviate much from a horizontal position and a slight smoothing in horizontal direction is justified.

3.3 Complementary geophysical data: Transient electromagnetic and seismic refraction methods

3.3.1 Transient electromagnetic soundings

Transient electromagnetic (TEM) soundings were used to gain information about vertical variations of the electrical

TABLE 2 Number of TEM soundings in each profile (with profile 1 starting in the south) and indication if overlapping measurements were performed (i.e., subsequent TEM loops overlap).

Profile	Number of soundings	Overlap
1	51	complete profile
2	63	complete profile
3	55	partly overlapping
4	37	partly overlapping
5	29	-
6	27	-
7	25	-
8	24	-
9	25	-
10	29	partly overlapping
11	31	partly overlapping
12	24	-
13	25	-
14	24	-
15	23	-
16	23	-

properties across the study area. Measurements were conducted using a single-loop geometry, where the same cable is used as transmitter and receiver, typically in a closed square or circular geometry. The method is based on the circulation of a direct current in the transmitter loop, which generates a primary magnetic field. The abrupt switch-off of the direct current induces eddy currents into the subsurface. This system of eddy currents decays over time and generates the secondary magnetic field (Ward and Hohmann, 1988). The temporal variations of this secondary magnetic field are measured in the receiver loop in terms of a voltage that is sampled along logarithmically distributed time windows. Since the measured decay of the secondary magnetic field depends on the subsurface electrical resistivity, inverse modelling can be used to reconstruct resistivity changes at depth along 1D profiles below the sounding position (e.g., Christiansen et al. (2006)).

Single-loop TEM data was collected along 16 profiles for a total of 517 soundings between the 1st and 4th June in 2018 using a TEM-FAST 48 manufactured by AEMR (Applied Electromagnetic Research). We used a circular loop with a radius of approx. 4 m for a cable length of 25 m (i.e., transferring to a square loop of 6.25 m side length) and a 12 V power source with a 1 A direct current, corresponding to a magnetic momentum of 39 Am², to collect the data. The voltage decay was sampled along 24 time windows up to 256 μ s after current shut-off and we used a total stacking of 9,984 transients to increase the signal to noise ratio. The average sounding spacing was about 8 m except for the southern part of the study area where overlapping measurements were performed (i.e., a loop center separation of 4 m; cf. Table 2 and Figure 2B).

The location of each sounding was determined with an RTK-GNSS.

Preprocessing of the TEM data consisted of a visual inspection of the TEM soundings and a manual removal of erroneous voltage readings, i.e., readings that deviate from the expected smooth decay or negative voltage readings. Early-time readings up to 25 μ s were particularly affected by noise likely related to an enhanced turn-off ramp effect caused by a highly conductive ($< 0.5 \Omega$) loop cable (Aigner et al., 2021). Therefore, the first 10 time gates of each sounding were removed from the entire data set. Furthermore, we filtered additional readings in the late-times depending on the observed curve smoothness and the presence of negative voltage readings. 1D sections of the vertical changes of electrical resistivity were obtained by inverting the data with ZondTEM1D (Kaminsky, 2001) using a smoothness-constraint regularization. To permit a fair discretization over the entire model depth, a model with 16 layers with fixed thickness was chosen. Using a number of layers in the model much larger than the actual number of lithological layers observed in the boreholes permits a fair discretization in the inversion. We then evaluated the data fit and removed additional voltage readings where the measured data was not fitted by the inverted model.

3.3.2 Refraction seismic tomography

The refraction seismic method (RST) is based on the propagation and refraction of artificially generated seismic waves in the subsurface and the measurement of ground motion in order to measure travel times of the refracted waves between the shot point and geophone locations. Such travel times can then be inverted to construct a continuous model of the subsurface velocity of P-waves, which depends on the density and the elastic properties of the material (Lankston, 1990). Contrasts in P-wave velocity can be used to infer the contact between unconsolidated sediments and the bedrock. (Leucci et al., 2007; Parasnis, 2012).

To support the interpretation of the electrical results, 10 RST profiles (Figure 2C) were measured between 12th to 16th June in 2017 and between 23rd to 26th April in 2019. Summit seismic recorders (by DMT, Germany) with 24 channels were used to record the seismic wave-field. For our surveys we deployed 30 Hz vertical geophones and collected 1,024 ms traces with a sampling of 1/4 ms. A 5 kg sledgehammer was used as a seismic source and a stack of three shots was made at each geophone location. Table 3 presents the orientation of each profile, as well as the corresponding number of geophones and geophone spacing. The signal processing, consisting of a low-pass filter and an amplitude amplification, and the first break picking were performed with code developed by M. Steiner at the TU Wien. The refraction module of pyGIMLi (Rücker et al., 2017) was subsequently used to invert the travel times to recover 2D sections of seismic velocity using a smoothness-constraint inversion scheme.

TABLE 3 Number of deployed geophones, the geophone spacing, the orientation and year of collection of the seismic profile.

Profile	Number of geophones	Geophone spacing [m]	Orientation	Year collected
1	96	2.5	E-W	2019
2	72	3	E-W	2019
3	72	3	E-W	2019
4	72	3	N-S	2019
5	72	2.25	N-S	2019
6	48	1.2	N-S	2019
7	48	3	E-W	2017
8	48	3	E-W	2017
9	48	3	E-W	2017
10	72	2.5	N-S	2017

TABLE 4 Drilled depth, performed laboratory investigations and associated number of samples in each borehole. The mineralogical investigations included both bulk rock and clay mineralogy.

Borehole	Number of samples			Drilled depth in m
	Grain size distribution and mineralogy	Cation exchange capacity	Plasticity	
WUR01	11	4	-	30
WUR02	6	2	4	16
WUR03	9	4	-	20
WUR04	7	3	-	20
WUR05	10	6	7	22

3.4 Borehole data

In April of 2017, five boreholes were drilled across the study area (Figure 2D) in depths varying between 16 and 30 m (cf. Table 4). For each borehole, coring was performed with a diameter of 180 mm and the retrieved sediments were stored for subsequent laboratory analysis and geological description. The lithological composition of the boreholes was similar and featured sediments of the Hausruck, Ampflwang and Otnang formation and materials of the first two formations were found to be variably disturbed and mixed due to past landslide processes.

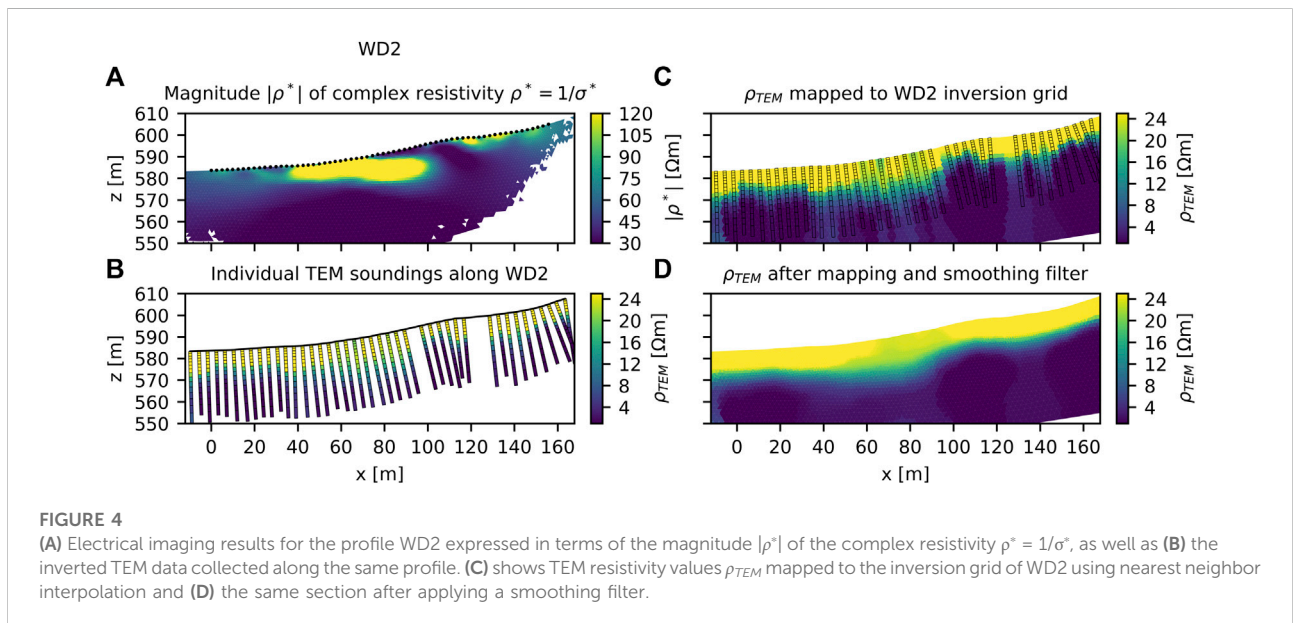
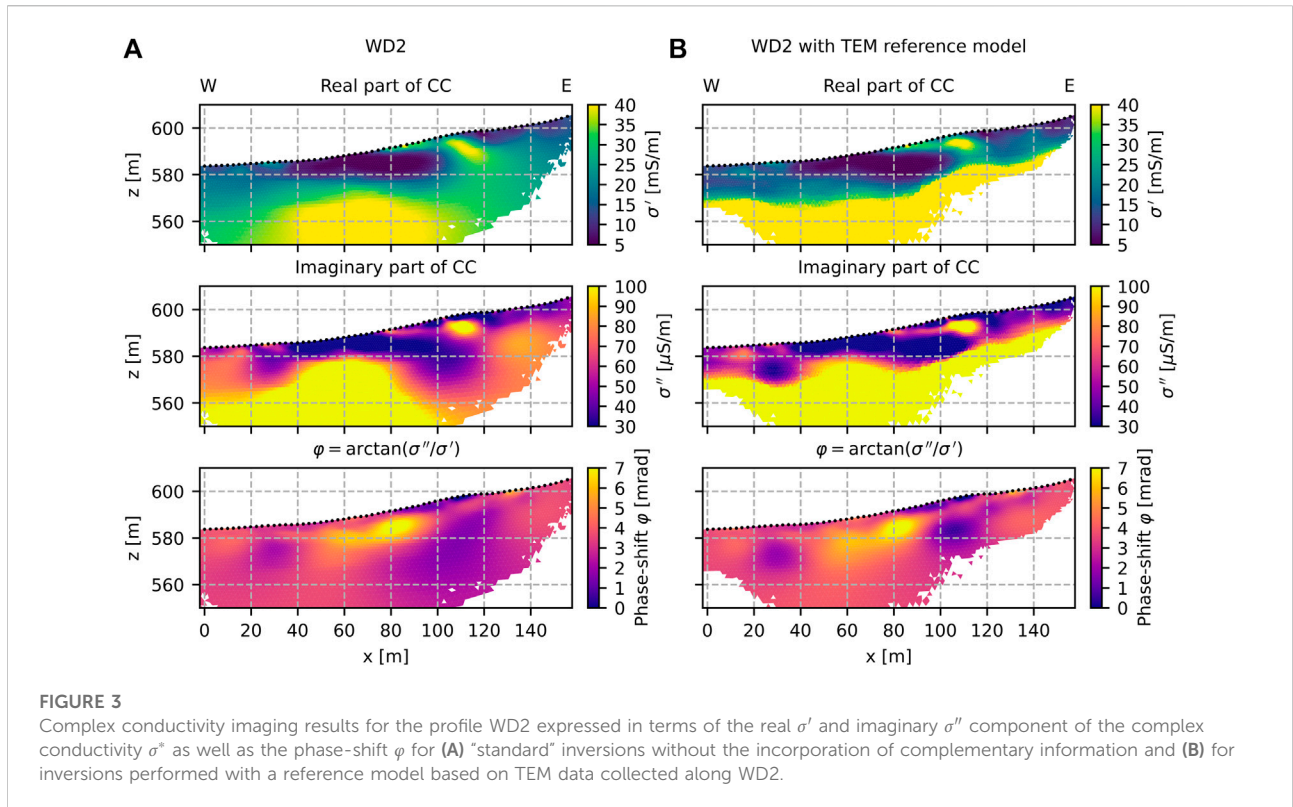
After the drilling of the boreholes, electromagnetic well-log measurements were conducted at each location using a Dual Induction Probe (by Robertson Geologging Ltd., UK), including continuous logs of the natural gamma radiation and apparent conductivity (Spies, 1996). Gamma logging is a widely used methodology to investigate formations (Schnyder et al., 2006) as specific minerals and sediments, such as feldspar, clays and shales host a larger number of radionuclides (Thorium, Potassium and Uranium) that emit gamma rays. Hence, gamma logs were used here to aid in the interpretation of clay-rich layers. Yet, the occurrence of organic matter might impose limitations on its interpretation (Myers and Wignall, 1987).

In total, 43 samples of the predominant layers within the core were probed and analyzed at the Geological Survey of Austria. The analysis included: 1) bulk rock mineralogy and clay mineralogy (< 2 μm fraction) determined by XRD (PANalytical X'Pert Pro Powder), 2) grain size distribution based on a combined analysis of wet sieving and Sedigraph (< 0.032 mm), and 3) cation exchange capacity (CEC) together with a chemical analysis of major and trace elements. CEC was determined with the barium chloride method (ÖNORM L 1086-1). Moreover, 11 samples were tested on their liquid and plastic limits at a certified testing laboratory (TPA, Vienna). Table 4 presents the number of samples and their distribution for each borehole.

4 Results

4.1 Improving electrical imaging results by incorporating a TEM based reference model

Figure 3A presents the CC imaging results for the profile WD2 (cf. Figure 2A) expressed in terms of the real σ' and imaginary σ'' components of the complex conductivity σ^* as



well as the phase-shift ϕ of the complex conductivity. Both the real and imaginary component reveal three main features, which can be described, from shallow to depth, as: 1) a shallow anomaly characterized by low conductivity ($\sigma' > 15$ mS/m) and polarization ($\sigma'' < 30$ μ S/m) values between 40 and 100 m

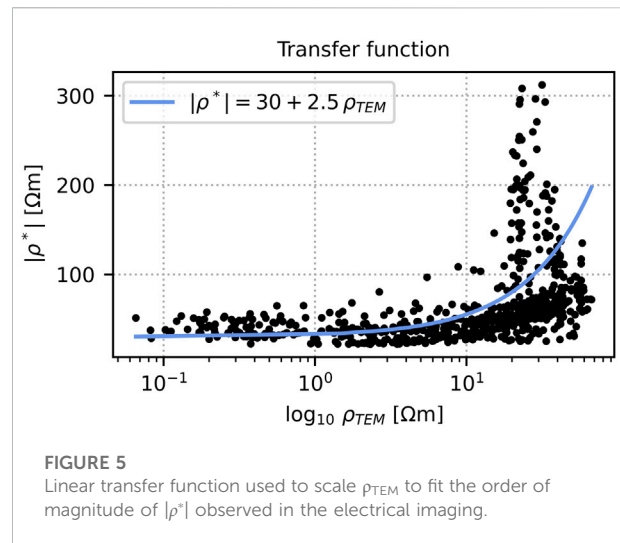
with a thickness varying between 5 and 10 m, 2) a spatially limited anomaly between 100 and 120 m characterized by increased σ' values above 40 mS/m and σ'' values above 100 μ S/m, and 3) a conductive and polarizable ($\sigma' > 40$ mS/m, $\sigma'' > 100$ μ S/m) unit below 1) and 2). The electrical images in

Figure 3A reveal electrical units that are roughly horizontal, yet lateral variations are observed, which cannot be easily explained from the geological background of the site but are assumed to be related to slope processes and resulting redistribution and deformation of slope sediments.

Figure 4B presents the inverted TEM models collected along the same profile. The TEM models indicate practically only two layers: a shallow one with resistivity values larger than $20 \Omega\text{m}$ and a thickness of 5–10 m, whereas a low resistivity layer ($\rho_{\text{TEM}} < 8 \Omega\text{m}$) can be found below it. Compared to the CCI images, the TEM results provide an increased contrast at depths larger than 12 m and at the edges of the CCI profile. The contact to materials with high electrical conductivity (and therefore low resistivity) cannot be resolved with a standard inversion of the CCI data, which favors smooth variations in both lateral and vertical direction.

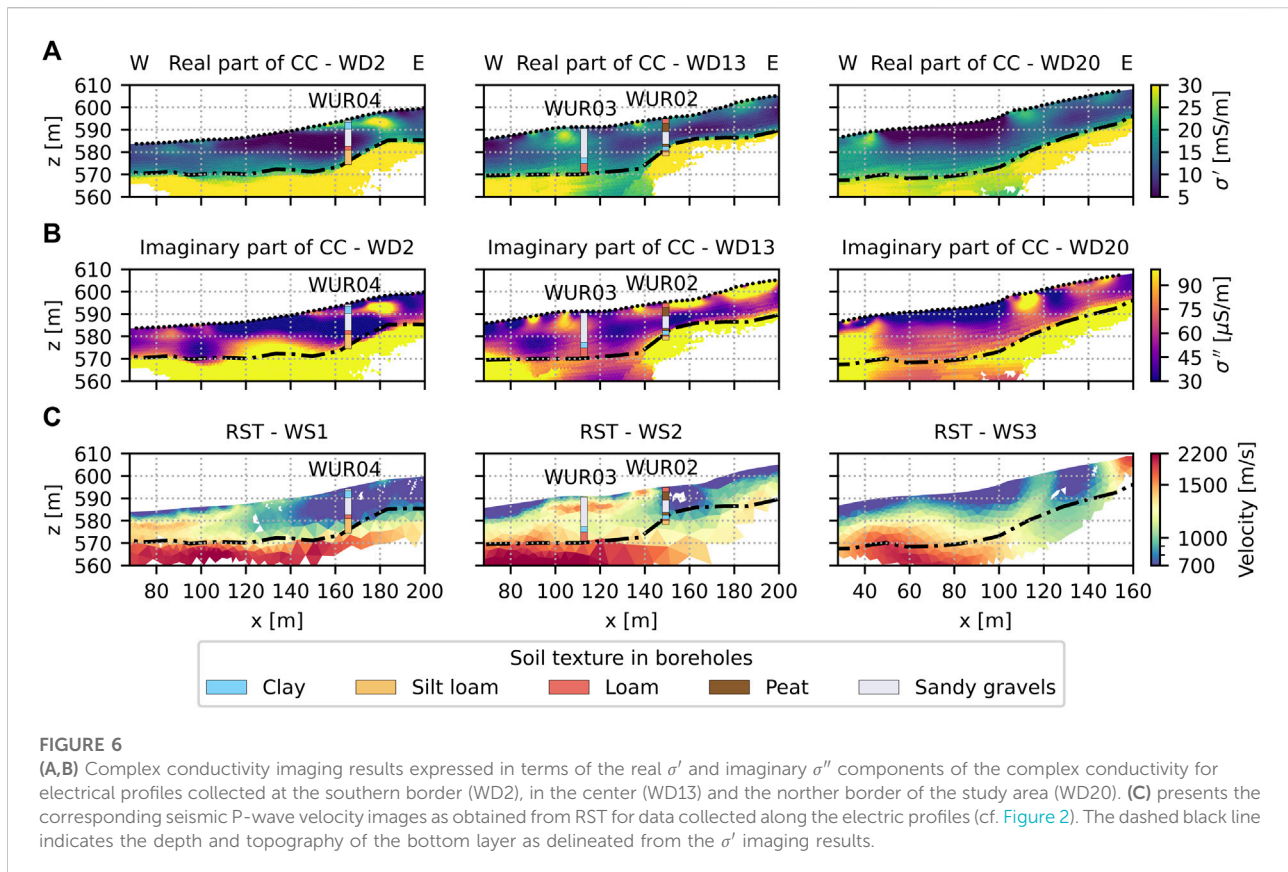
TEM inversion results have been used to support the interpretation of ERT and to a lesser extent CCI, for instance to delineate regional aquifer geometry (Meier et al., 2014), to trace saline contamination due to coastal salt water intrusion (Balía and Viezzoli, 2015; Ardali et al., 2018) and to investigate karst lakes (Bücker et al., 2021). Caterina et al. (2014) have shown that the incorporation of prior information in the inversion can help to obtain a more geologically plausible subsurface model. This can be achieved by modifying the regularization operator to account for a reference model (e.g., Oldenburg and Li, 1994) and was done for example by Catt et al. (2009) using EM data from a ground conductivity meter. Hence, we use the inverted TEM model as a reference model for the inversion of the CCI data in order to enhance the horizontal layering and to improve the vertical contrast between the electrical units. Other studies have proposed a joint inversion, where ERT and TEM data are solved simultaneously for the same resistivity model (e.g., Martínez-Moreno et al., 2017; Christensen 2022). However, the inclusion of CCI data in such scheme is beyond the scope of this manuscript.

For the construction of the TEM reference model, in a first step, we selected those TEM soundings that are located along to the CCI profiles. We note here that the inverted 1D TEM resistivity models are always considered to be perpendicular to ground surface; thus, these are tilted to account for the topography changes and mapped to the inversion mesh using nearest neighbor interpolation. Yet, due to the nature of the nearest neighbor interpolation, the so obtained models are not smooth (Figure 4C) and would likely lead to implausible inversion results. Hence, we perform a topography constrained bounding box to smooth the TEM models. Accordingly, for each model cell, we define a rectangular bounding box with given x - and z -axis lengths (32 and 12 m; i.e., 2.6:1 smoothing) which is then rotated based on the slope of the topography. After that, the median value of all model cells inside the bounding box is computed and



reassigned to a second mesh. We use a second mesh for the reassignment to avoid mutual dependencies of the smoothing outcome due to the sequence of model cells selected. Figure 4D presents the final reference model after mapping of the TEM values and the smoothing procedure revealing a “smooth” resistivity model.

The resistivity models from CCI and TEM are consistent, as observed in Figure 4A and Figure 4B, thus permitting to incorporate the electrical layer distribution computed for the TEM data (Figure 4C) as described above. Following this approach, we obtain the model presented in Figure 4D. The comparison of the models in Figure 4A and Figure 4D shows consistent models with variations in the magnitude of the electrical resistivity values. Such discrepancy is related to the different volumes for each measurement (i.e., quadrupoles with an electrode separation of 2.5 m when compared with a transmitter loop with an area of 39 m^2 , e.g., Auken et al., 2006). To overcome this, we scaled the resistivity values retrieved from the inversion of TEM data by the computation of a transfer function. In detail, we extracted the $|\rho^*|$ values from the inverted CCI section at the location of the tilted TEM soundings, and computed a linear regression as presented in Figure 5. We used individual transfer functions for each electrical profile. Furthermore, we investigated the use of the reference model without a rescaling of the resistivity values, which revealed only minimal changes in the solved images compared to the rescaled ones, as expected, considering that during the inversion the actual resistivity values are fitted to the measured data and the reference model only aids within the regularization (Caterina et al., 2014). Hereafter, we refer only to CCI results obtained using a reference model in the inversion based on the rescaled TEM model. We note here that we used a homogeneous half space with $\varphi = 0$ for the impedance phase of



the reference model. In Figure 3B, we present the CCI images for the profile WD2 after inversion with the TEM reference model. As it can be seen in Figure 3B (bottom row), the use of a homogeneous reference model for the phase-shift has only minor effects on the obtained phase-shift image. A comparison with Figure 3A also shows that small scale lateral changes in shallow depths (e.g., the polarizable anomaly, with $\sigma'' > 100 \mu\text{S/m}$, at 110 m along the profile) are preserved while solving for a continuous layer with an increased contrast at depth.

4.2 Using CC imaging and RST to delineate subsurface architecture

We present in Figure 6 the seismic P-wave velocity and improved CC imaging results for profiles located at the southern border, in the center and at the northern border of the study area (Figure 2). Moreover, to evaluate the seismic and electrical response in comparison to actual soil-physical properties, we present lithological logs overlapping the seismic and CC imaging results. The lithological logs correspond to the soil textural analysis of subsurface materials recovered during the drilling of the boreholes WUR02 and WUR03 collocated to the profile WD13 and borehole WUR04 collocated to profile WD2.

Images of the real conductivity σ' presented in Figure 6A, in general, reveal two electrical units consisting of a conductive layer in the bottom ($\sigma' > 30 \text{ mS/m}$) and a less conductive layer on the top ($5 > \sigma' < 30 \text{ mS/m}$). The interface between the two layers lies at a depth of 15–20 m, with lateral variations not necessarily following the changes of the surface topography, as evidenced, for instance, in the abrupt change observed in WD13 between 140 and 180 m along the profile direction. The top layer generally reveals σ' values between 5 and 30 mS/m and is characterized by small-scale lateral σ' changes in shallow depths that can be observed between 150 and 180 m in WD2 and between 90 and 110 m in WD13. Images of the imaginary conductivity σ'' , as presented in Figure 6B, reveal similar features, namely a two-layer model with a polarizable bottom layer ($\sigma'' > 100 \mu\text{S/m}$) and low polarizable top layer ($\sigma'' < 70 \mu\text{S/m}$). Low polarization in the top layer could be linked to previously mobilized materials, as for instance, reported by Flores Orozco et al. (2018a). In such study, the authors argue that low compaction and low saturation in sliding materials leads to a low polarization response. Yet, σ'' imaging results for WD13, when compared to σ' , reveal spatially limited polarizable anomalies in shallow depths, particularly visible from 135 m on. Moreover, the σ'' bottom layer in WD2 shows a distinct anomaly between 120 and 150 m that is not visible in the corresponding σ' image.

To facilitate the comparison between the CCI and RST results, the interface between the two electrical units in the σ' images, as described above, is superimposed in RST images. These RST images reveal consistent features to those observed in the σ' images, i.e., a two-layer model comprised of a bottom layer with velocities larger than 2,200 m/s, likely associated to consolidated sediments; whereas the top layer reveals velocities between 700 and 1,500 m/s, likely associated to previously mobilized materials. In general, the depth and topography of the bottom layer resolved by the RST is in agreement with the electrical images. However, particularly to the end of the seismic profiles (e.g., from 160 m on for WS1 and from 140 m on for WS2) differences in the seismic and electrical images can be observed. The convex anomaly in the σ' images is not resolved in the seismic sections, which indicate a more concave structure. We explain such differences by changes in the composition of the bottom layer, which does not necessarily provide the same response in seismic and electrical measurements. For instance, we interpret such differences as an increase in clay content, a factor that does not necessarily represent an increase in seismic velocity, which is more sensitive to changes in compaction/consolidation. Furthermore, shallow anomalies within the top layer that reveal high seismic velocity ($> 1,500$ m/s), as for example visible in WS2 between 100 and 140 m, are also consistent with anomalies observed in the σ'' images ($\sigma'' > 100 \mu\text{S/m}$). Such anomalies reveal an existing heterogeneity in the shallow subsurface properties, possibly related to lenses with compacted materials, which again, could point to previous landslide events and corresponding dislocation of lithological formations. Alternatively, such heterogeneities could indicate the start of undisturbed slope sediments in the foreland of the landslide (cf. Figure 1C).

The layered model interpreted from both the σ' and σ'' images can be fairly tied to the borehole information (cf. Figure 6), yet the polarization image (σ'') yields a better agreement with the borehole data. Here, the conductive and polarizable bottom layer can be related to fine-grained sediments (clay, silt loam and loam), whereas the sandy gravels are represented by a low polarization response and low conductivity values ($\sigma'' < 70 \mu\text{S/m}$ and $\sigma' < 20 \text{ mS/m}$). Moreover, the shallow polarizable units ($\sigma'' > 100 \mu\text{S/m}$) observed between 110 and 170 m along WD13 are in agreement with peat as observed in WUR02, which is a material known for its high polarization response (Slater and Reeve, 2002; Comas and Slater, 2004; Katona et al., 2021). Differences in the lateral changes of the interface between the top and bottom layer, as retrieved from seismic and electric methods for WD13 and WS2 between 140 and 200 m along the profile can now be explained by a change in texture from loam to silt loam, and the likely associated change in soil moisture, both factors that will probably not affect the seismic velocity as significantly as it does the complex conductivity.

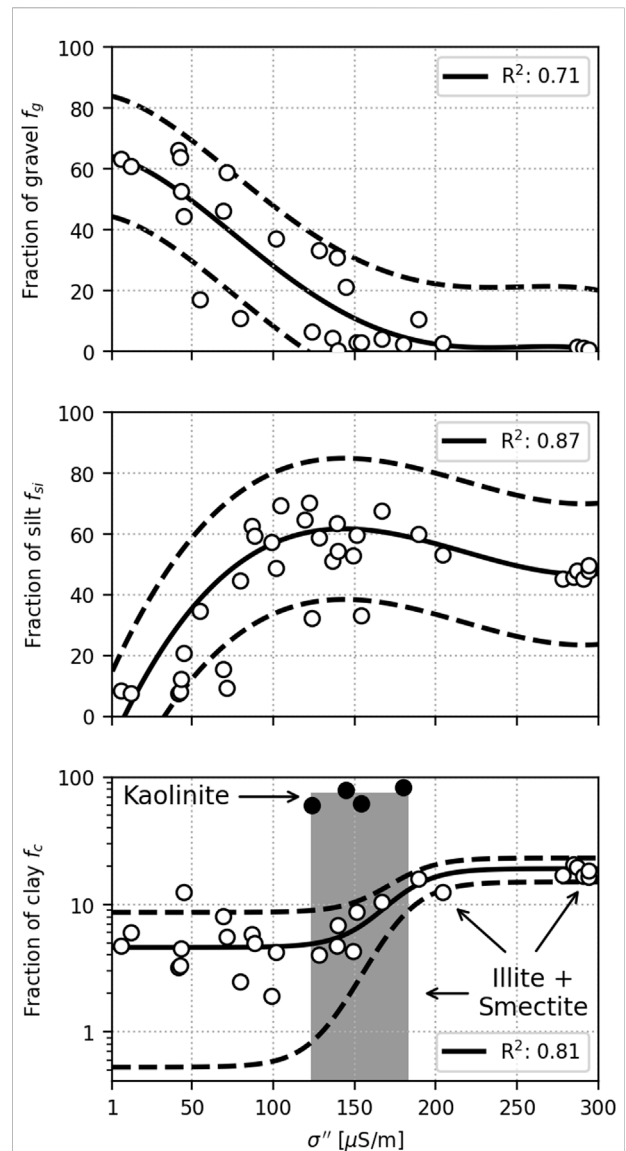


FIGURE 7

Scatter plots of the imaginary conductivity σ'' (white circles) and volume fraction of gravel (top) and silt (center) and clay (bottom) reveal well-determined relationships, with the adjusted regression functions (black line) reaching R^2 scores > 0.7 . The black dashed line indicates the confidence bounds computed for two times the standard deviation of the corresponding regression function.

4.3 Site-specific correlations between soil-physical parameters and the imaginary conductivity: A potential for upscaling to spatial continuous information

We observe a fair qualitative agreement between borehole information and the inverted electrical data. Hence, in a first step, we extracted the model parameters from the electrical images at

the depth and location of the boreholes. The extracted model parameters are computed as the median value of a k -nearest neighbor search (with k being five elements of the electrical model) and the starting point for the search being the depth and location of the borehole relative to the profile. In a second step, we correlated the available soil-physical and extracted electrical model parameters. For this analysis, we only used borehole data from the wells WUR01, WUR02, WUR03 and WUR05, while the information corresponding to well WUR04 will be used in a later step to evaluate the retrieved petrophysical models. For the sake of brevity, we only present the most significant correlations that are later on discussed in the upscaling approach.

Our analysis revealed that the most significant correlations were observed between the grain size distribution (i.e., the different soil volume fractions of gravel f_g , sand f_{sa} , silt f_{si} and clay f_c) and the polarization response expressed in terms of the imaginary component of the complex conductivity σ'' . Accordingly, in Figure 7 we present the imaginary conductivity σ'' plotted against f_g , f_{si} and f_c , as well as the adjusted regression functions and their confidence bounds. The σ'' - f_g scatter plot reveals a negative correlation, more precisely, an approximately linear decrease in gravel fraction in the polarization range between 1 and 175 $\mu\text{S/m}$ (σ''), from which on the gravel fraction remains constant at 1–3%, and hence, independent of σ'' . We model this nonlinear relationship with a high degree polynomial function that writes

$$f_g = -4.069 \times 10^{-8}(\sigma'')^4 + 2.661 \times 10^{-5}(\sigma'')^3 - 4.615 \times 10^3(\sigma'')^2 - 0.125\sigma'' + 64.21 \quad (6)$$

and fits our data to a reasonable R^2 score of 0.71. The σ'' - f_{si} scatter plot reveals a more complex relationship, that is, a nonlinear increase in silt fraction in the range between 1 and 150 $\mu\text{S/m}$ (σ''), where the silt fraction reaches its maximum of about 70%, and, a moderate decrease in silt fraction for σ'' values larger than 150 $\mu\text{S/m}$. We found that a cubic function captures the characteristics of the described relationship fairly well with a R^2 score of 0.87 and the obtained function writes as:

$$f_{si} = 9.458 \times 10^{-6}(\sigma'')^3 - 6.165 \times 10^{-3}(\sigma'')^2 + 1.186\sigma'' - 9.614. \quad (7)$$

Finally, σ'' plotted against the log-converted fraction of clay f_c indicates two regimes. On the one hand, 1) a narrow band of clay fractions above 70% corresponding to σ'' between 120 and 170 $\mu\text{S/m}$; while on the second hand 2) a step response for clay fractions below 30% that is characterized by low contents of clay ($< 7\%$) for σ'' below 120 $\mu\text{S/m}$, and moderately increased clay content up to 20–25% for σ'' values above 170 $\mu\text{S/m}$. The analysis of the clay mineralogy revealed clear differences in the fraction of kaolinite, smectite and illite, with an abundance of kaolinite for regime 1) and a combined percentage over 70% of smectite and illite for regime

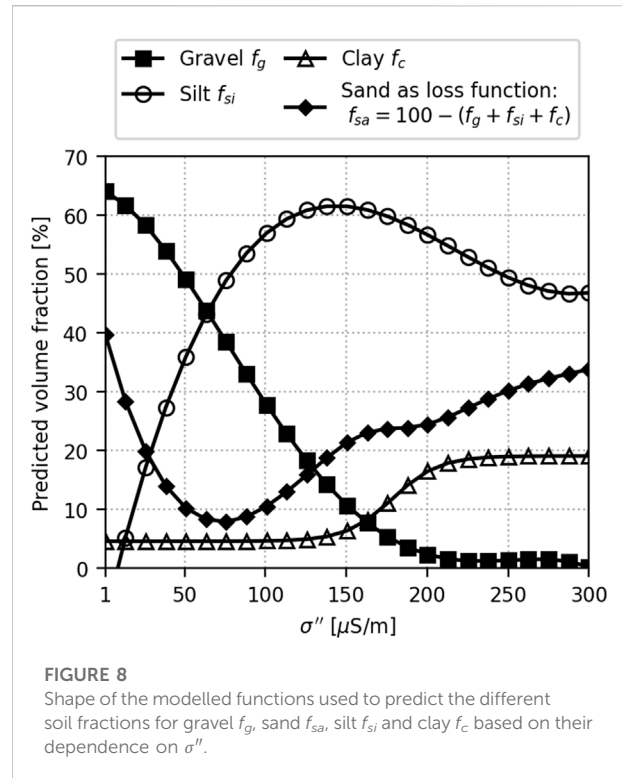


FIGURE 8 Shape of the modelled functions used to predict the different soil fractions for gravel f_g , sand f_{sa} , silt f_{si} and clay f_c based on their dependence on σ'' .

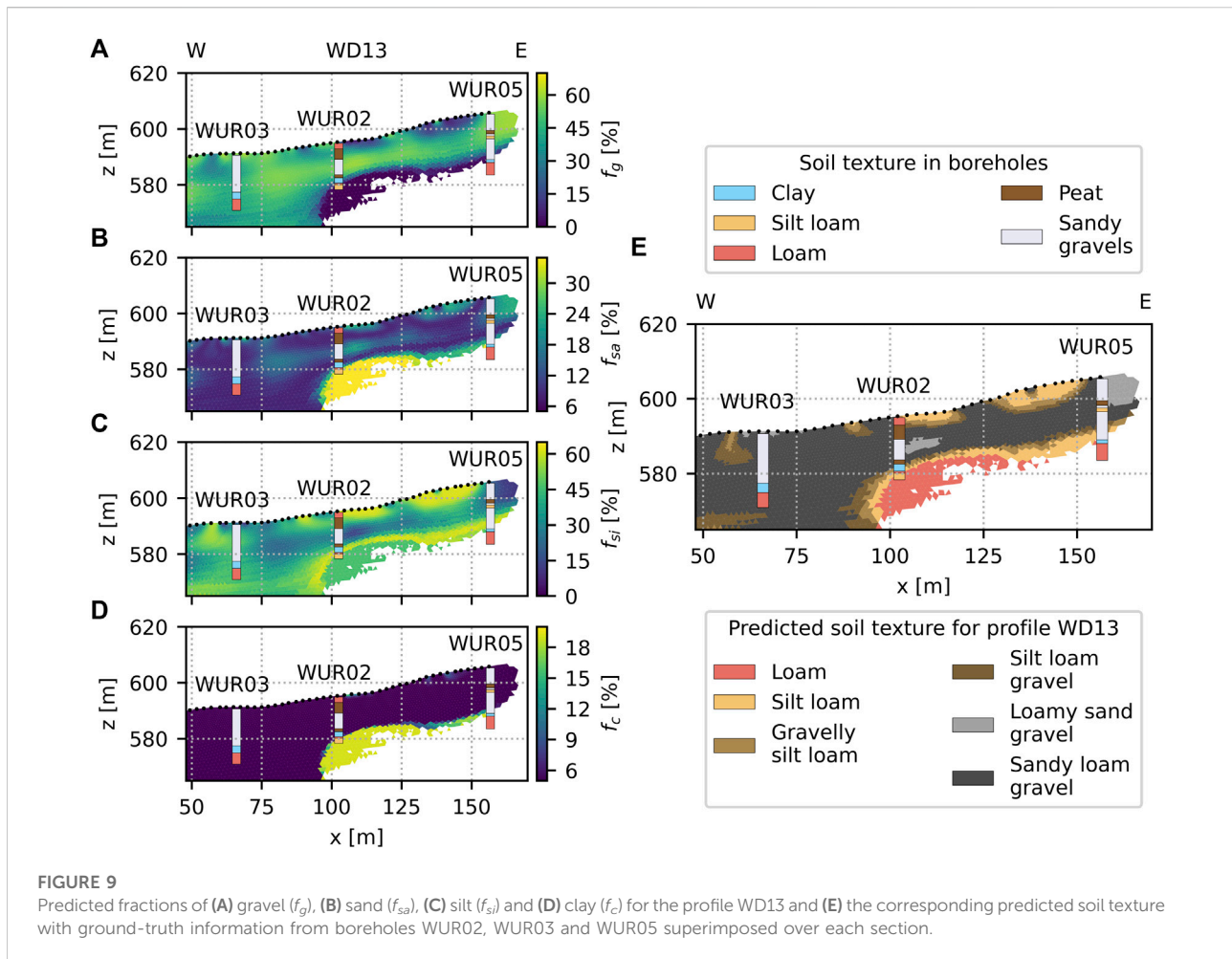
2) As previously discussed by e.g., Leroy and Revil (2009), Okay et al. (2014) and Lévy et al. (2018), there is a dependence of the polarization response on the type of dominant clay mineral. Hence, we explain the observed changes in σ'' for the clay fraction associated to variations in clay mineralogy. Since only 4 out of 36 samples were associated to kaolinite we decided to omit them and only model the response for regime 2) with a logistic function that adjusts the data to a R^2 score of 0.81. Hence, the σ'' - f_c function can be written as:

$$f_c = 14.5 \left(1 + e^{-0.07\sigma'' + 12.5} \right)^{-1} + 4.6 \quad (8)$$

The correlation of σ'' - f_{sa} did not reveal any clear relationship. Hence, we determine the missing sand fraction f_{sa} as a loss function, knowing that all fractions combined should add up to 100%.

$$f_{sa} = 100 - (f_g + f_{si} + f_c) \quad (9)$$

Implicitly, this approach also ensures that the total fraction is always capped at 100%. Figure 8 presents the shape of the prediction functions for f_g , f_{si} , f_c , as well as f_{sa} as a loss function. In general, we predict coarser textures (sand and gravel) for σ'' below 75 $\mu\text{S/m}$, mostly silt for the middle range ($75 > \sigma'' > 200 \mu\text{S/m}$) and a mixture of sand, silt and clay for σ'' larger than 200 $\mu\text{S/m}$.



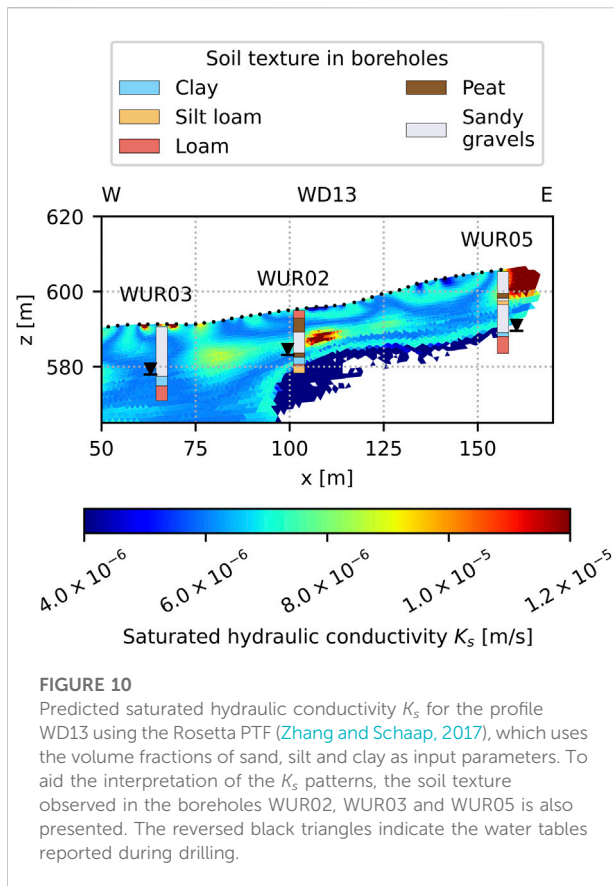
4.4 Quantification of soil-textural and hydraulic properties in a complex conductivity imaging framework

Given the relationships that link the imaginary conductivity to soil fractions, we now have a practical tool to upscale from borehole information (i.e., retrieved samples from drilling) to spatially continuous information over the entire study area. In Figure 9, we use the Equations (6)–(9) for the estimation of gravel, silt, clay and sand from the electrical imaging results from profile WD13 across the entire imaging plane. Based on the soil classification system (NRCS, 1993 - from the United States Department of Agriculture, USDA), we include a classification of soil texture in Figure 9, as well as the soil texture reported from the core analysis of the boreholes WUR02, WUR03 and WUR05.

The comparison of borehole and electrical data reveals a good agreement between the predicted and reported soil textures, with exception of the deep fine-grained units in WUR03. For the hydrogeological interpretation of our results, we now define two

main units. A top layer, from the surface to a depth varying between 12 and 18 m, which consists of sandy gravels intercalated by peat, loam and silt loam. Below there is a bottom layer, characterized mostly by fine-grained sediments. Such bottom layer consists of a thin clay unit on top of loam and silt loam. In terms of the stratigraphy, the top layer can be related to the Hausruck formation, whereas the bottom layer corresponds to the Ampflwang and Ottnang formation respectively. Albeit mixtures of different formations, due to past landslide events, can be expected in both layers.

Soil hydraulic properties are preferred over soil texture alone as it provides direct information about water flow. Hence, in a second step, we investigate the possibility to retrieve hydraulic conductivity estimates in an imaging framework built on the quantitative correlation of geophysical and borehole data. We used the recent adaption of Rosetta (Zhang and Schaap, 2017) to estimate K_s (along with the VG parameters) from our predicted soil fractions. As Rosetta uses the volume fractions of sand, silt and clay as input with the requirement that the fractions sum up to 100% soil volume, we had to modify our sand prediction



function. Accordingly, our sand prediction (f_{sa}) accounts for both sand and gravels, such as:

$$f_{sa} = 100 - (f_{si} + f_c) \quad (10)$$

In particular, Eq. (10) predicts larger fractions of sand for $\sigma'' < 150 \mu\text{S/m}$ (cf. Figure 8). We argue that this could be used as a first proxy for the missing gravel fraction, i.e., increasing the fraction of the next smallest grain size class.

Figure 10 presents the resulting K_s distribution for WD13 applying Rosetta to our data. For completeness, the VG parameters as well as the soil texture classification when using the adapted sand computation are presented in the (Figure A1). In general, the predicted K_s values are roughly distributed over two orders of magnitude (4.0×10^{-6} to 1.0×10^{-5} m/s) with largest values observed for gravelly textures in the top layer, e.g., at the location of WUR02 and WUR05. At depth, the model predicts the lowest K_s values ($K_s < 4.0 \times 10^{-6}$ m/s) that seem to trace the layers of clay, loam and silt loam in WUR02 and WUR05.

WUR03 shows only moderate K_s values (6.0×10^{-6} m/s). As depicted in Figure A1, the overall texture in WD13 is dominated by loamy components (silt loam and sandy loam), which is also reflected in the predicted homogeneous K_s values.

In this context, both lateral and vertical variations, e.g., at WUR02, can be explained by either a higher portion of sand that leads to an increase of $K_s > 8.0 \times 10^{-6}$ m/s, or larger fractions of silt corresponding to a decrease in $K_s < 7.0 \times 10^{-6}$ m/s.

Considering the implications of the K_s prediction on the slope hydrogeology, the bottom layer with K_s values below 4.0×10^{-6} m/s is expected to act as hydraulic barrier for interflow, whereas the top layer can be considered as an unconfined aquifer that permits infiltration of surface water. This interpretation is supported by water tables reported during drilling, which were found at the depth of the clay layer or slightly above it (as depicted in Figure 10). Interflow along the interface between bottom and top layer will likely result in weathering of slope materials (i.e., the dissolution and accumulation of fine grains) and, therefore, development of weathered loam.

4.5 Preferential water-flow paths and their implication on slope morphology

We have shown that for WD13 the hydrogeological system is governed by practically two layers: an unconfined aquifer with a thickness of 12–18 m on top of a unit with low hydraulic conductivity. Hence, in a next step we investigated how the interface topography changes for the entire study area, as well as the possibility to delineate possible preferential water-flow paths based on a combined interpretation of the interface topography and the geomorphological surface features.

The comparison of Figure 6 and Figure 10 clearly shows that the transition from low to high σ'' values at depth (from 40 to $> 90 \mu\text{S/m}$) also marks the transition to the lowest K_s values ($< 4.0 \times 10^{-6}$ m/s). Thus, we compute the interface geometry for the entire study area. To achieve this, we manually extracted the interface in the σ'' images in all profiles. For those profiles that resolved a discontinuous interface in the CC, we included the analysis of the transition from P-wave velocity from 1,500 to 2,200 m/s for the location of the discontinuity. The obtained interfaces were converted from 2D coordinates to their respective 3D coordinates using an affine transformation, with a subsequent interpolation to a uniform 3.6 m grid using the kriging method to obtain a quasi-continuous model.

Figure 11 shows the so obtained aquiclude interface for the entire study area as well as the DEM hillshade with a color-coded surface elevation overlay. Furthermore, to aid the interpretation of the topographical changes of the aquiclude interface, the gradient vector magnitude in each grid cell is also presented. In general, the interface reveals a decrease in the elevation from east to west consistent to the surface elevation. However, clear differences can be observed in the eastern part of the study area ($X > 25,050$ m) where the interface reveals a much steeper

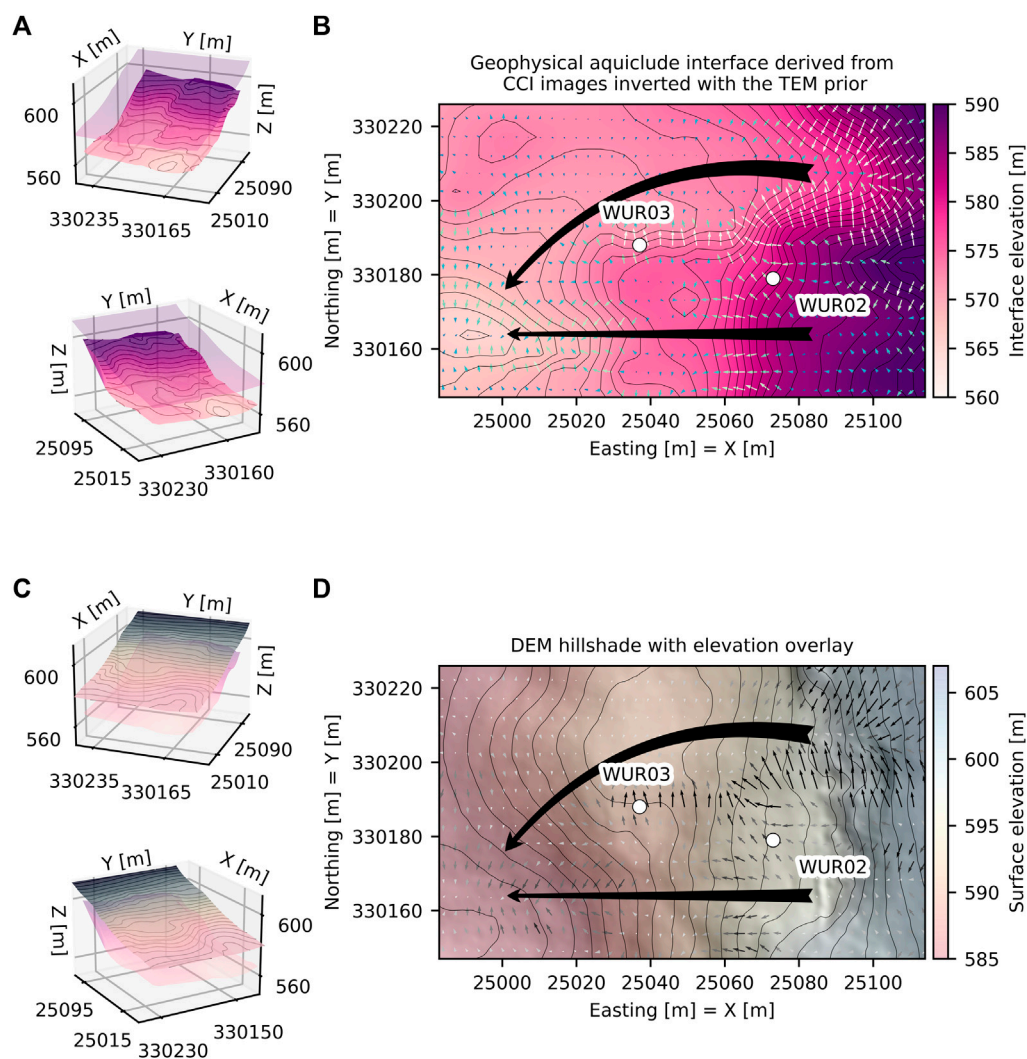


FIGURE 11

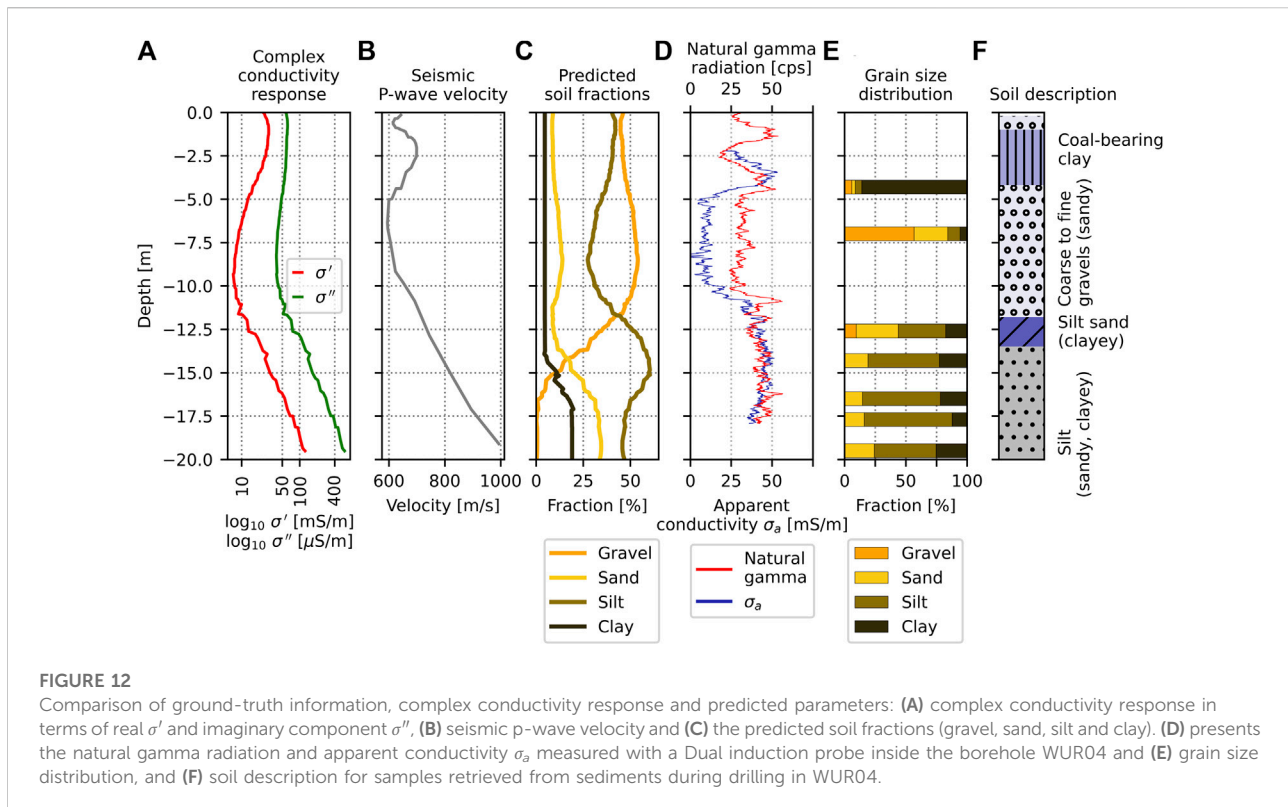
Aquiclude interface derived from combination of CCI (using the TEM reference model) and RST in **(A)** 3D representation (grey shading indicates the DEM) and **(B)** as map with the corresponding gradient vector magnitudes (small regularly distributed and color-coded arrows) and interpreted preferential water-flow paths (black arrows) superimposed on it. **(C)** and **(D)** present the corresponding 3D view and map of the color-coded surface topography, again superimposing both the gradient vectors magnitudes and preferential flow paths from the aquiclude map.

dipping (i.e., densely grouped isolines) compared to surface topography.

In a similar manner, the surface topography shows a bulge north-west of WUR03; whereas the interface topography indicates a depression. Based on the isolines and gradient magnitudes of the interface layer, we propose two possible preferential water-flow paths, as depicted in Figure 11. In particular, Figure 11 shows 1) a channel starting in the north-eastern part of the study area and continuing north of WUR03 to the south-western part of the study area; and, 2) a roughly direct channel from the south-eastern to the south-western part of the study area. The pathway 1) can clearly be traced by the form of the isolines and gradient vector magnitudes

which indicate a depression and likely channeling of interflow, while for pathway 2) a small bulge for the eastern part ($X > 25,060$ m) and a more pronounced depression of the western part ($X < 25,040$ m) can be observed. Both 1) and 2) seem to merge in a common location (roughly at $X=24,990$ m, $Y=330,165$ m).

Figure 11 indicates that the largest surface topographical changes are associated to those locations where the topography of the interface exhibits the largest gradient vector magnitudes, particularly visible in the eastern part of the study area. We argue that the channeling of interflow through preferential flow paths will likely accelerate weathering or changes in pore-pressure and, therefore,



could promote subsidence in those particular areas. Following this argumentation, the bulge in the surface topography northwest of WUR03 is interpreted as deformation of the plastic-reacting slope sediments or materials of a former mudflow as a reaction of the uplift pressure of the main landslide (cf. Figure 1C). To attenuate this effect, a possible counter-measure could include extending the drainage system downslope below the former source/waterlogged area. This could mitigate the channeling of subsurface water-flow along the interface topography.

5 Discussion

Figure 9 and Figure 10 demonstrate the ability of the geophysical data to recover subsurface heterogeneity regarding the variations in textural parameters. We propose the combination of geophysical data with Rosetta for the estimation of subsurface hydraulic conductivity in an imaging framework. However, to properly evaluate the accuracy of our approach, it is necessary to compare the estimated values with independent data. To this end, we evaluate here the textural parameters estimated at the position of the borehole WUR04, where ground-truth data is available but was not used for the calibration of petrophysical parameters conducted above.

Figure 12 shows the complex conductivity and seismic velocity extracted from the inversion results (obtained for WD4 and WS1) and the predicted soil fractions at the location of WUR04 as well as borehole data (grain size of recovered samples, natural gamma radiation and conductivity logging). The geophysical data was obtained from an extraction box with a width of 1.5 m. For the prediction of textural parameters, we computed the moving average of the quadrature 1D profile (σ''). This is due to the higher amount of data points in the extraction box near to the surface scattering over a larger range than values at depth. The higher amount is stemming from the denser discretization of the inversion grid in the vicinity of the electrode locations.

For the predicted soil fractions, we observe a good agreement for the gravels, especially at the depth of 7.5 m, where both the predicted and the measured grain size indicate a fraction of gravel of 50%, with the content of coarse materials decreasing at 12.5 m depth, and becomes negligible at a depth of 16 m. The predicted fraction of silt below 12.5 m depth is in line with the measured values in soil samples; however, our model appears to slightly overestimate the silt content (approx. 10%) for the sandy gravels at 7.5 m depth. Accordingly, our model predicts ca. 10% less sand content for the layer at 7.5 m depth. The prediction of clay content reveals a constant value of 5% from the surface to a depth

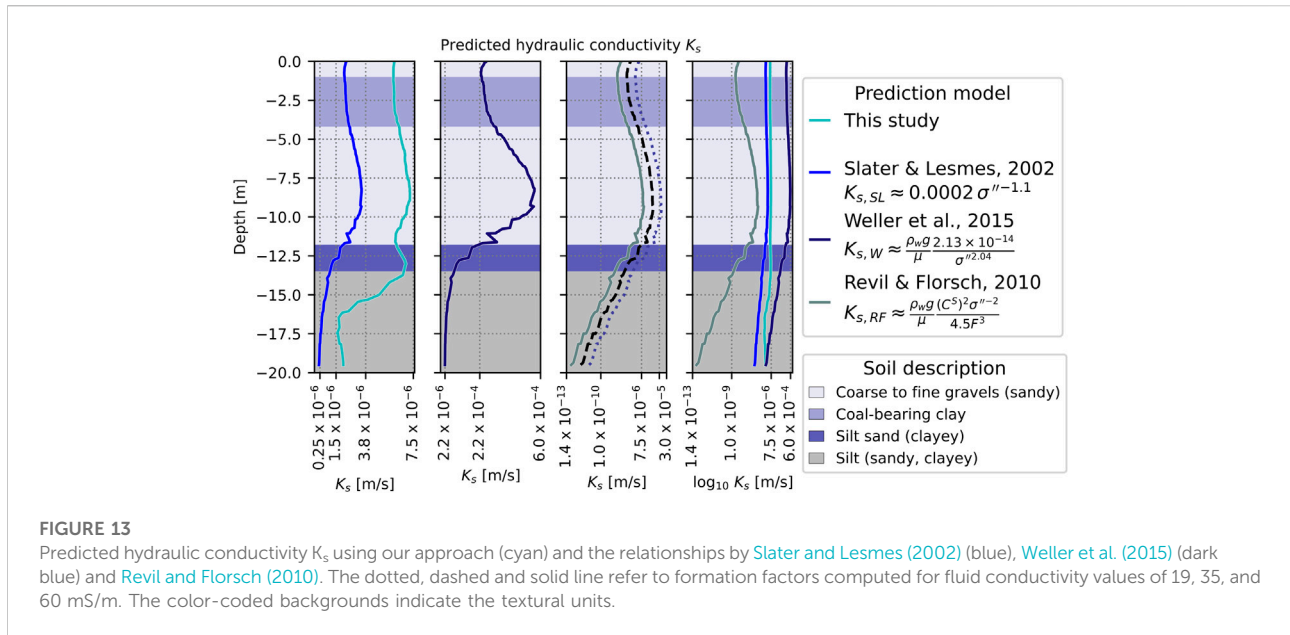


FIGURE 13

Predicted hydraulic conductivity K_s using our approach (cyan) and the relationships by Slater and Lesmes (2002) (blue), Weller et al. (2015) (dark blue) and Revil and Florsch (2010). The dotted, dashed and solid line refer to formation factors computed for fluid conductivity values of 19, 35, and 60 mS/m. The color-coded backgrounds indicate the textural units.

of ~13 m, where it increases to a value of 20%, which is in agreement with the values reported from the analysis of samples. However, the clay-rich layer (clay > 85%) at 4.5 m is not resolved in our prediction. As previously mentioned, in our correlation function (Equation (8)) we decided to exclude large clay fractions related to kaolinite, as they seem to be clustered in a single location. Accordingly, our approach is not able to predict clay fractions larger than 20%. Considering that such high clay contents are only rarely observed, the approach proposed represents the best compromise to simplify our model linking the polarization response (σ'') and the textural parameters.

The predicted K_s profile presented in Figure 13 shows intermediate values ($K_s \sim 5.0 \times 10^{-6}$ m/s) between (roughly) 0.5 and 4 m depth, where the seismic velocity data shows maximum values around 700 m/s corresponding to a coal-bearing clay layer occurring at this depth. The velocity maximum likely indicates a higher degree of compaction for the clay layer, in turn explaining the low hydraulic conductivity values resolved. Below 4 m depth, our prediction shows the largest values ($K_s > 5.0 \times 10^{-6}$ m/s) associated to sandy gravels (gravel fraction 50%) down to a depth of 12 m and a smooth transition to slightly lower values ($K_s < 2.0 \times 10^{-6}$ m/s) for the silt layer (with a combined clay and silt content above 75%) below 12 m depth. Moreover, below 12 m depth the seismic velocity increases from 600 m/s to 1,000 m/s, which indicates an increase in compaction, in agreement with the estimated K_s values. Between 10 and 12.5 m depth, the estimated K_s indicates a slight decrease that could be related to a clay-rich lens. Although no analysis was conducted on samples of this particular location, the natural gamma indicates a significant

spike at this depth, similar to the one associated to the coal-bearing clay layer mentioned above, therefore sustaining the resolved change in the K_s values.

Besides the evaluation of our estimations with independent data from borehole WUR04, we also compare our estimated K_s prediction with hydraulic conductivity values computed using existing $\sigma'' - K_s$ relationships. Such relationships have been obtained from laboratory studies where both the complex conductivity and the hydraulic conductivity have been measured in small samples, yet in fully saturated conditions. In particular, we compare our K_s values to those computed with the model by Slater and Lesmes (2002) and the one proposed by Weller et al. (2015). The former is based on a Hazen-type equation (Hazen, 1911), and can be written as:

$$K_{s,SL} \approx 0.0002\sigma''^{-1.1} \tag{11}$$

In their study, Weller et al. (2015) investigated 38 unconsolidated soil samples, demonstrating an inversely linear correlation between σ'' and the permeability k for data collected at 1 Hz. Such model can be written as (Weller et al., 2015):

$$k_W^* \approx \frac{2.14 \times 10^{-14}}{\sigma''^{2.04}} \tag{12}$$

In this study we used a dynamic viscosity ($\mu = 0.0010518$) and density ($\rho = 998.59$) for water at 18°C and an acceleration due to gravity ($g = 9.8073$) to transform the permeability values k^* to hydraulic conductivity values $K_{s,W}$. For the sake of completeness, we also computed the hydraulic conductivity values using the model by Revil and Florsch (2010), which also links the imaginary component σ'' to hydraulic conductivity, based on the relationship written as:

$$K_{s,RF} \approx \frac{\rho_w g (C^S)^2 \sigma''^{-2}}{\mu 4.5 F^3} \quad (13)$$

in which C^S is the specific conductance of the Stern Layer assumed equal to 4×10^{-9} and F the electrical formation factor describing the ratio between tortuosity and porosity (Katz and Thompson, 1987). Following the approach by Weller et al. (2010), we used a first order approximation for the computation of F based on the ratio of the bulk conductivity (σ_0) to fluid conductivity (σ_w), such as

$$F = \frac{\sigma_w}{\sigma_0} \quad (14)$$

In our case, σ_0 was given by the real component of the complex conductivity (σ') and σ_w to three different values equal to 19, 35 and 60 mS/m, corresponding to values observed in monitoring stations around the study site. The comparison of the different K_s predictions is presented in Figure 13.

$K_{s,SL}$ estimates are consistent to those predicted by our approach; however, $K_{s,SL}$ values fluctuate around 1.0×10^{-6} m/s, representing one order of magnitude smaller than our predictions. Actually, vertical variations of the $K_{s,SL}$ values are identical down to a depth of 10 m, for the unconsolidated materials with coarse grains. At this depth $K_{s,SL}$ monotonously decreases with depth; whereas our prediction shows two peaks, one related to high hydraulic conductivity values (between ~12 and 14 m depth) and the lowest values resolved between 16 and 17.5 m depth corresponding to the clayey silt layer. Since the $K_{s,SL}$ estimation is a direct function of σ'' , it can only capture the dynamics resolved in the σ'' distribution. In this regard, the mismatch between the two estimates below 10 m depth is due to the two-step approach proposed, where the polarization values (σ'') are used first to estimate the soil fractions, which are subsequently included in Rosetta for the K_s predictions. On the opposite, the $K_{s,SL}$ model uses a single-step approach, where the polarization is inversely related to the hydraulic conductivity as presented in Equation (11). Binley et al. (2016) also noted that sites with relatively low contrast in K are expected to exhibit low structural resolution of the complex conductivity distribution. In this regard, our approach permits to resolve for a larger dynamic in the predicted hydraulic conductivity values as these are estimated from the soil fractions and not directly from the inverted complex conductivity.

The use of the model proposed by Weller et al. (2015) shows a larger range of hydraulic conductivity values (between 2.2×10^{-6} and 6.0×10^{-4} m/s). However, such variability cannot easily be understood in the study area, where high contents of fine grains are also observed in the top layer. Moreover, the $K_{s,W}$ cannot resolve for the increase in the hydraulic conductivity resolved at the contact between the silt sand and the silt (ca. 13 m depth). Similar to the approach by Slater and Lesmes (2002), the model by Weller et al. (2015) is only related to the changes in the polarization (σ''); thus, it is not sensitive to changes in the grain size underlying our approach. We believe

that discrepancies in the values obtained between the $K_{s,SL}$, $K_{s,W}$ and our approach are mainly due to the use of fitting parameters that cannot be extrapolated from laboratory to field scale, where large heterogeneities dominate, in contrast to well-sorted laboratory samples. In this case, our approach offers the possibility to experimentally fit the hydraulic conductivity to the polarization response through Rosetta and, thus, consider subsurface variations and existing ground truth. Moreover, it needs to be taken into account that the models by Slater and Lesmes (2002) and Weller et al. (2015) are based on measurements in fully saturated samples, whereas our measurements are conducted in materials with varying water content. In this regard, the applicability of the $K_{s,SL}$ and $K_{s,W}$ models may be hindered for field investigations in slopes characterized by clay rich sediments, where water flow rather occurs along preferential water flow paths. We also note here that laboratory measurements of the CC are commonly conducted on small soil samples; thus, unable to capture the response due to the presence of coarse sediments as those observed in our study area.

Albeit the discrepancies observed in Figure 13, the three methods (Slater and Lesmes (2002); Weller et al. (2015) and our approach) solve for the same maximum between 7.5 and 10 m depth, which corresponds to the gravels and the low polarization response. For the sake of completeness, we also present estimated values using the model proposed by Revil and Florsch (2010) based on the polarization of the Stern layer. Such model results in hydraulic conductivity values much lower than the rest of the predictions. Such discrepancy may be explained by the rough estimation of the formation factor due to the lack of more detailed information. It seems that the crude approximation, based on the ratio of the fluid-to-bulk conductivity (Equation 14), fails to solve for adequate F values, resulting in inaccurate estimations of the hydraulic conductivity. In this regard, the use of equations with less parameters (e.g., the one by Slater and Lesmes, 2002) provides clear advantages for field investigations. Accordingly, our approach permits to estimate hydraulic conductivity based solely on geophysical data and grain size analysis, which is one of the common measurements in landslide investigations. Further methods requiring of measures of the formation factor, or other parameters may be limited to areas where such information is available.

As previously stated, Rosetta can only be applied to SSC data and therefore the initial set-up did not incorporate training data containing gravel fractions. Further studies may investigate the use of more complex PTFs that permit the incorporation of the gravel fraction. However, originating from soil science, most readily available PTFs are restricted to SSC only (Van Looy et al., 2017). Hence, we believe that our approach offers a flexible tool able to quantify hydraulic conductivity variations at the field-scale based on complex conductivity imaging results. It is important to note that the use of the complex conductivity permits to explicitly take the

surface conductivity into account, which may explain high conductivity values in clayey areas. Hydraulic estimations based only on real-valued electrical resistivity, may fail to account for surface conductivity, misinterpreting clay rich formations as areas with high water content. The application of the two-step approach proposed here (first the soil fraction and only then the K_s values) seems to account for existing ground truth data, for subsurface heterogeneity as well as variations in the geophysical properties (complex conductivity and to certain extent seismic velocities). Therefore, our approach may represent a step forward in the upscaling of the relationship between σ'' and K that has been observed in different investigations (see [Kemna et al., 2012](#)).

6 Conclusion

We have shown that complex conductivity imaging permits to solve for changes in electrical properties consistent with lithological contacts recovered from boreholes. The lithological units resolved in our study correspond to, from top to bottom: a layer with moderate conductivity values ($5 > \sigma' < 30$ mS/m) and an average thickness of 15 m on top of a conductive bottom layer ($\sigma' > 30$ mS/m). This model is supported by information about electrical units, as obtained from TEM soundings, and RST imaging results. The extensive complex resistivity data permitted to construct a 3D subsurface model, which is then used to delineate the geometry of an aquiclude as well as preferential water-flow paths within the slope. Based on the spatial variations of the hydraulic conductivity (K_s) solved, we can also identify a spatial correlation between the aquiclude interface and the morphological features. In this regard, our hydrogeophysical model offers a possibility to design adequate measures to attenuate build-up of pore-pressure along preferential flow paths that may trigger landslides.

We present a quantitative interpretation of the complex conductivity images, using both soil-textural data and well-logging information. Within this study we derive site-specific petrophysical relationships that link the imaginary complex conductivity to the fractions of gravel, silt and clay. These well-determined relationships—with R^2 scores of 0.71 for gravel, 0.87 for silt and 0.81 for clay—permitted to estimate the textural properties of the resolved geophysical units, which were found consistent to grain size distribution measured in soil samples recovered from core drilling. The textural information was used in the Rosetta pedo-transfer function to predict K_s from the complex conductivity imaging results. Hence, an estimation of hydraulic conductivity values was obtained for the entire study area.

The application of the two-step approach proposed here (i.e., first the soil fraction and then the K_s values) provides comparable values to those computed using existing

petrophysical equations developed from laboratory investigations. Such petrophysical equations consider the polarization response at 1 Hz yet are based on measurements typically performed on small, well sorted samples under fully saturated conditions. Therefore, those equations may be limited in field applications, associated to large degrees of heterogeneity and variations in water content. Hence, the approach proposed here permits to derive K_s based solely on available data, namely complex conductivity and grain size distributions, without the need to upscale petrophysical equations resolved in the laboratory.

Data availability statement

The raw data supporting the conclusion of this article will be made available by the authors, without undue reservation.

Author contributions

JG, AF contributed to conception and design of the study. MP, JB organized the soil-physical database. JG, AF, LA performed the processing of the geophysical data. JG wrote the first draft of the manuscript. AF, DS, MP, and LA wrote sections of the manuscript. All authors contributed to manuscript revision, read, and approved the submitted version.

Funding

This work is supported through the Austrian Science Fund (FWF)—Agence Nationale de la Recherche (ANR) research project I 2619-N29 and ANR-15-CE04-0009-01 HYDRO-SLIDE: Hydro-geophysical observation for an advanced understanding of clayey landslides.

Conflict of interest

The authors declare that the research was conducted in the absence of any commercial or financial relationships that could be construed as a potential conflict of interest.

Publisher's note

All claims expressed in this article are solely those of the authors and do not necessarily represent those of their affiliated organizations, or those of the publisher, the editors and the reviewers. Any product that may be evaluated in this article, or claim that may be made by its manufacturer, is not guaranteed or endorsed by the publisher.

References

- Aigner, L., Högenauer, P., Bucker, M., and Flores-Orozco, A. (2021). A flexible single loop setup for water-borne transient electromagnetic sounding applications. *Sensors* 21 (19), 6624. doi:10.3390/s21196624
- Alvioli, M., Melillo, M., Guzzetti, F., Rossi, M., Palazzi, E., von Hardenberg, J., et al. (2018). Implications of climate change on landslide hazard in Central Italy. *Sci. total Environ.* 630, 1528–1543. doi:10.1016/j.scitotenv.2018.02.315
- Ardali, A., S., Tezkan, B., and Güreç, A. (2018). On the salt water intrusion into the durusu lake, istanbul: A joint central loop TEM and multi-electrode ERT field survey. *Pure Appl. Geophys.* 175 (8), 3037–3050. doi:10.1007/s00024-018-1813-1
- Auken, E., Pellerin, L., Christensen, N. B., and Sørensen, K. (2006). A survey of current trends in near-surface electrical and electromagnetic methods. *Geophysics* 71 (5), G249–G260. doi:10.1190/1.2335575
- Balia, R., and Viezzoli, A. (2015). Integrated interpretation of IP and TEM data for salinity monitoring of aquifers and soil in the coastal area of Muravera (Sardinia, Italy). *Boll. Geofis. Teor. Appl.* 56, 31. doi:10.4430/bgta0136
- Balting, D. F., AghaKouchak, A., Lohmann, G., and Ionita, M. (2021). Northern Hemisphere drought risk in a warming climate. *npj Clim. Atmos. Sci.* 4 (1), 61–13. doi:10.1038/s41612-021-00218-2
- Ban, N., Schmidli, J., and Schär, C. (2015). Heavy precipitation in a changing climate: Does short-term summer precipitation increase faster? *Geophys. Res. Lett.* 42 (4), 1165–1172. doi:10.1002/2014gl025888
- Baumann, S., Robl, J., Prasicsek, G., Salcher, B., and Keil, M. (2018). The effects of lithology and base level on topography in the northern alpine foreland. *Geomorphology* 313, 13–26. doi:10.1016/j.geomorph.2018.04.006
- Berg, A., Sheffield, J., and Milly, P. C. (2017). Divergent surface and total soil moisture projections under global warming. *Geophys. Res. Lett.* 44 (1), 236–244. doi:10.1002/2016gl071921
- Binley, A., Hubbard, S. S., Huisman, J. A., Revil, A., Robinson, D. A., Singha, K., et al. (2015). The emergence of hydrogeophysics for improved understanding of subsurface processes over multiple scales. *Water Resour. Res.* 51 (6), 3837–3866. doi:10.1002/2015wr017016
- Binley, A., Keery, J., Slater, L., Barrash, W., and Cardiff, M. (2016). The hydrogeologic information in cross-borehole complex conductivity data from an unconsolidated conglomeratic sedimentary aquifer. *Geophysics* 81 (6), E409–E421. doi:10.1190/geo2015-0608.1
- Binley, A., and Kemna, A. (2005). “Dc resistivity and induced polarization methods,” in *Hydrogeophysics* (Springer), 129–156.
- Binley, A., and Slater, L. (2020). *Resistivity and induced polarization: Theory and applications to the near-surface earth*. Cambridge University Press.
- Blume, T., and Van Meerveld, H. J. (2015). From hillslope to stream: Methods to investigate subsurface connectivity. *WIREs Water* 2 (3), 177–198. doi:10.1002/wat2.1071
- Bogaard, T. A., and Greco, R. (2016). Landslide hydrology: From hydrology to pore pressure. *WIREs Water* 3 (3), 439–459. doi:10.1002/wat2.1126
- Bücker, M., Flores Orozco, A., and Kemna, A. (2018). Electrochemical polarization around metallic particles — Part 1: The role of diffuse-layer and volume-diffusion relaxation. *Geophysics* 83 (4), E203–E217. doi:10.1190/geo2017-0401.1
- Bücker, M., Flores Orozco, A., Undorf, S., and Kemna, A. (2019a). On the role of stern-and diffuse-layer polarization mechanisms in porous media. *J. Geophys. Res. Solid Earth* 124 (6), 5656–5677. doi:10.1029/2019jb017679
- Bücker, M., Undorf, S., Flores Orozco, A., and Kemna, A. (2019b). Electrochemical polarization around metallic particles—Part 2: The role of diffuse surface charge. *Geophysics* 84 (2), E57–E73. doi:10.1190/geo2018-0150.1
- Bücker, M., Flores Orozco, A., Gallistl, J., Steiner, M., Aigner, L., Hoppenbrock, J., et al. (2021). Integrated land and water-borne geophysical surveys shed light on the sudden drying of large karst lakes in southern Mexico. *Solid earth*. 12 (2), 439–461. doi:10.5194/se-12-439-2021
- Campbell, R. H. (1975). *Soil slips, debris flows, and rainstorms in the santa monica mountains and vicinity, southern California*. U.S. Professional Paper. Govt. Print. Off. (USGS Numbered Series no. 851).
- Catt, L. M., West, L. J., and Clark, R. A. (2009). The use of reference models from a priori data to guide 2D inversion of electrical resistivity tomography data. *Geophys. Prospect.* 57 (6), 1035–1048.
- Caterina, D., Hermans, T., and Nguyen, F. (2014). Case studies of incorporation of prior information in electrical resistivity tomography: Comparison of different approaches. *Near Surf. Geophys.* 12 (4), 451–465. doi:10.3997/1873-0604.2013070
- Christensen, N. B. (2022). Joint inversion of airborne TEM data and surface geoelectrical data. The Egebjerg case. *J. Appl. Geophys.* 196, 104511. doi:10.1016/j.jappgeo.2021.104511
- Christiansen, A. V., Auken, E., and Sørensen, K. (2006). “The transient electromagnetic method,” in *Groundwater geophysics* (Springer), 179–225.
- Comas, X., and Slater, L. (2004). Low-frequency electrical properties of peat. *Water Resour. Res.* 40 (12), 3534. doi:10.1029/2004wr003534
- Cook, B. I., Mankin, J. S., and Anchukaitis, K. J. (2018). Climate change and drought: From past to future. *Curr. Clim. Change Rep.* 4 (2), 164–179. doi:10.1007/s40641-018-0093-2
- Cosby, B., Hornberger, G., Clapp, R., and Ginn, T. (1984). A statistical exploration of the relationships of soil moisture characteristics to the physical properties of soils. *Water Resour. Res.* 20 (6), 682–690. doi:10.1029/wr020i06p0682
- Cruden, D. M., and Varnes, D. J. (1996). “Landslide types and processes,” in *Landslides: Investigation and mitigation*. Editors A. K. Turner and R. L. Schuster (Transportation Research Board, Special Report 247, National Research Council), 36–75.
- Dahlin, T., and Zhou, B. (2006). Multiple-gradient array measurements for multichannel 2d resistivity imaging. *Near Surf. Geophys.* 4 (2), 113–123. doi:10.3997/1873-0604.2005037
- Doetsch, J., Ingeman-Nielsen, T., Christiansen, A. V., Fiandaca, G., Auken, E., and Elberling, B. (2015). Direct current (dc) resistivity and induced polarization (ip) monitoring of active layer dynamics at high temporal resolution. *Cold Regions Sci. Technol.* 119, 16–28. doi:10.1016/j.coldregions.2015.07.002
- Dunn, R. J., Alexander, L. V., Donat, M. G., Zhang, X., Bador, M., Herold, N., et al. (2020). Development of an updated global land *in situ*-based data set of temperature and precipitation extremes: HadEX3. *J. Geophys. Res. Atmos.* 125 (16), e2019JD032263. doi:10.1029/2019jd032263
- Flores Orozco, A., Williams, K. H., Long, P. E., Hubbard, S. S., and Kemna, A. (2011). Using complex resistivity imaging to infer biogeochemical processes associated with bioremediation of an uranium-contaminated aquifer. *J. Geophys. Res.* 116 (G3), G03001. doi:10.1029/2010jg001591
- Flores Orozco, A., Bücker, M., Steiner, M., and Malet, J.-P. (2018a). Complex-conductivity imaging for the understanding of landslide architecture. *Eng. Geol.* 243, 241–252. doi:10.1016/j.enggeo.2018.07.009
- Flores Orozco, A., Gallistl, J., Bücker, M., and Williams, K. H. (2018b). Decay curve analysis for data error quantification in time-domain induced polarization imaging. *Geophysics* 83 (2), E75–E86. doi:10.1190/geo2016-0714.1
- Flores Orozco, A., Micic, V., Bücker, M., Gallistl, J., Hofmann, T., and Nguyen, F. (2019). Complex-conductivity monitoring to delineate aquifer pore clogging during nanoparticles injection. *Geophys. J. Int.* 218 (3), 1838–1852. doi:10.1093/gji/ggz255
- Flores-Orozco, A., Gallistl, J., Steiner, M., Brandstätter, C., and Fellner, J. (2020). Mapping bio-geochemically active zones in landfills with induced polarization imaging: The heferlbach landfill. *Waste Manag.* 107, 121–132. doi:10.1016/j.wasman.2020.04.001
- Flores Orozco, A., Aigner, L., and Gallistl, J. (2021). Investigation of cable effects in spectral induced polarization imaging at the field scale using multicore and coaxial cables. *Geophysics* 86 (1), E59–E75. doi:10.1190/geo2019-0552.1
- Gallistl, J., Weigand, M., Stumvoll, M., Ottowitz, D., Glade, T., and Orozco, A. F. (2018). Delineation of subsurface variability in clay-rich landslides through spectral induced polarization imaging and electromagnetic methods. *Eng. Geol.* 245, 292–308. doi:10.1016/j.enggeo.2018.09.001
- Godio, A., and Bottino, G. (2001). Electrical and electromagnetic investigation for landslide characterisation. *Phys. Chem. Earth, Part C Sol. Terr. Planet. Sci.* 26 (9), 705–710. doi:10.1016/s1464-1917(01)00070-8
- Grandjean, G., Gourry, J.-C., Sanchez, O., Bitri, A., and Garambois, S. (2011). Structural study of the ballandaz landslide (French alps) using geophysical imagery. *J. Appl. Geophys.* 75 (3), 531–542. doi:10.1016/j.jappgeo.2011.07.008
- Grunert, P., Soliman, A., C’oric, S., Scholger, R., Harzhauser, M., and Piller, W. E. (2010). Stratigraphic re-evaluation of the stratotype for the regional otnangian stage (central paratethys, middle burdigalian). *Newsl. Stratigr.* 44 (1), 1–16. doi:10.1127/0078-0421/2010/0001
- Hazen, A. (1911). Discussion: Dams on sand foundations. *Trans. Am. Soc. Civ. Eng.* 73 (11), 199–203.
- Hinsch, R. (2008). New insights into the oligocene to miocene geological evolution of the molasse basin of Austria. *OIL GAS-EUROPEAN Mag.* 34 (3), 138–143.

- Holmes, J., Chambers, J., Meldrum, P., Wilkinson, P., Boyd, J., Williamson, P., and Donohue, S. (2020). Four-dimensional electrical resistivity tomography for continuous, near-real-time monitoring of a landslide affecting transport infrastructure in British Columbia, Canada. *Near Surf. Geophys.* 18, 337–351. [Geoelectrical Monitoring](#).
- Huntley, D., Bobrowsky, P., Hendry, M., Macciotta, R., Elwood, D., Sattler, K., et al. (2019). Application of multi-dimensional electrical resistivity tomography datasets to investigate a very slow-moving landslide near Ashcroft, British Columbia, Canada. *Landslides* 16 (5), 1033–1042. doi:10.1007/s10346-019-01147-1
- Jorda, H., Bechtold, M., Jarvis, N., and Koestel, J. (2015). Using boosted regression trees to explore key factors controlling saturated and near-saturated hydraulic conductivity. *Eur. J. Soil Sci.* 66 (4), 744–756. doi:10.1111/ejss.12249
- Kaminsky, A. (2001). *Zondtem1d (zond software corporation)*.
- Katona, T., Gilfedder, B. S., Frei, S., Bücken, M., and Flores-Orozco, A. (2021). High-resolution induced polarization imaging of biogeochemical carbon-turnover hot spots in a peatland. *Biogeosciences* 2021, 4039–4058. doi:10.5194/bg-18-4039-2021
- Katz, A., and Thompson, A. (1987). Prediction of rock electrical conductivity from mercury injection measurements. *J. Geophys. Res.* 92 (B1), 599–607. doi:10.1029/jb092ib01p00599
- Kemna, A., Binley, A., Cassiani, G., Niederleithinger, E., Revil, A., Slater, L., et al. (2012). An overview of the spectral induced polarization method for near-surface applications. *Near Surf. Geophys.* 10 (6), 453–468. doi:10.3997/1873-0604.2012027
- Kemna, A. (2000). *Tomographic inversion of complex resistivity: Theory and application*. Osnabrück, Germany: Der Andere Verlag.
- Konapala, G., Mishra, A. K., Wada, Y., and Mann, M. E. (2020). Climate change will affect global water availability through compounding changes in seasonal precipitation and evaporation. *Nat. Commun.* 11 (1), 1–10. doi:10.1038/s41467-020-16757-w
- Krenmayr, H., and Schnabel, W. (2006). *Geological map of upper Austria, 1: 200,000*.
- Kušnirák, D., Dostál, I., Putiška, R., and Moješ, A. (2016). Complex geophysical investigation of the kapušany landslide (eastern Slovakia). *Contributions Geophys. Geodesy* 46 (2), 111–124. doi:10.1515/congeo-2016-0008
- LaBrecque, D. J., and Ward, S. H. (1990). Two-dimensional cross-borehole resistivity model fit ting. *Geotechnical Environ. Geophys.* 1, 51–57.
- Lankston, R. W. (1990). “High-resolution refraction seismic data acquisition and interpretation,” in *Geotechnical an environmental geophysics: Volume I: Review and tutorial* (Society of Exploration Geophysicists), 45–74. doi:10.1190/1.9781560802785.ch3
- Lehmann, P., Merlin, O., Gentine, P., and Or, D. (2018). Soil texture effects on surface resistance to bare-soil evaporation. *Geophys. Res. Lett.* 45 (19), 10–398. doi:10.1029/2018gl078803
- Leroy, P., and Revil, A. (2009). A mechanistic model for the spectral induced polarization of clay materials. *J. Geophys. Res.* 114, B10202. doi:10.1029/2008jb006114
- Leucci, G., Greco, F., De Giorgi, L., and Mauceri, R. (2007). Three-dimensional image of seismic refraction tomography and electrical resistivity tomography survey in the castle of occhiola (sicily, Italy). *J. Archaeol. Sci.* 34 (2), 233–242. doi:10.1016/j.jas.2006.04.010
- Lévy, L., Gibert, B., Sigmundsson, F., Fóvenz, Ó., Hersir, G. P., Briole, P., et al. (2018). The role of smectites in the electrical conductivity of active hydrothermal systems: electrical properties of core samples from Krafla volcano, Iceland. *Geophys. J. Int.* 215 (3), 1558–1582.
- Li, R., Hu, X., Xu, D., Liu, Y., and Yu, N. (2020). Characterizing the 3d hydrogeological structure of a debris landslide using the transient electromagnetic method. *J. Appl. Geophys.* 175, 103991. doi:10.1016/j.jappgeo.2020.103991
- Lin, Q., Wang, Y., Glade, T., Zhang, J., and Zhang, Y. (2020). Assessing the spatiotemporal impact of climate change on event rainfall characteristics influencing landslide occurrences based on multiple GCM projections in China. *Clim. Change* 162 (2), 761–779. doi:10.1007/s10584-020-02750-1
- Loke, M., Chambers, J., and Ogilvy, R. (2006). Inversion of 2d spectral induced polarization imaging data. *Geophys. Prospect.* 54 (3), 287–301. doi:10.1111/j.1365-2478.2006.00537.x
- Maierhofer, T., Hauck, C., Hilbich, C., Kemna, A., and Flores-Orozco, A. (2022). Spectral induced polarization imaging to investigate an ice-rich mountain permafrost site in Switzerland. *The Cryosphere* 16(5), 1903–1925..
- Martin, T., Günther, T., Flores Orozco, A., and Dahlin, T. (2020). Evaluation of spectral induced polarization field measurements in time and frequency domain. *J. Appl. Geophys.* 180, 104141. doi:10.1016/j.jappgeo.2020.104141
- Martinez-Moreno, F. J., Monteiro-Santos, F. A., Bernardo, I., Farzaman, M., Nascimento, C., Fernandes, J., et al. (2017). Identifying seawater intrusion in coastal areas by means of 1D and quasi-2D joint inversion of TDEM and VES data. *J. Hydrology* 552, 609–619. doi:10.1016/j.jhydrol.2017.07.026
- Meier, P., Kalscheuer, T., Podgorski, J. E., Kgotlhang, L., Green, A., Greenhalgh, S., et al. (2014). Hydrogeophysical investigations in the western and north-central Okavango Delta (Botswana) based on helicopter and ground-based transient electromagnetic data and electrical resistance tomography. *Geophysics* 79 (5), B201–B211. doi:10.1190/geo2014-0001.1
- Morelli, G., and LaBrecque, D. J. (1996). “Robust scheme for ert inverse modeling,” in *Symposium on the Application of Geophysics to Engineering and Environmental Problems Proceedings*, 629–638. doi:10.4133/1.2922327
- Mualem, Y., and Friedman, S. (1991). Theoretical prediction of electrical conductivity in saturated and unsaturated soil. *Water Resour. Res.* 27 (10), 2771–2777. doi:10.1029/91wr01095
- Myers, K. J., and Wignall, P. B. (1987). “Understanding jurassic organic-rich mudrocks—new concepts using gamma-ray spectrometry and palaeoecology: Examples from the kimmeridge clay of dorset and the jet rock of yorkshire,” in *Marine clastic sedimentology* (Springer), 172–189.
- Nemes, A., Rawls, W. J., and Pachepsky, Y. A. (2006). Use of the nonparametric nearest neighbor approach to estimate soil hydraulic properties. *Soil Sci. Soc. Am. J.* 70 (2), 327–336. doi:10.2136/sssaj2005.0128
- Nrcs, U. (1993). “Soil survey division staff (1993) soil survey manual.” *Soil conservation service* (US Department of Agriculture Handbook), 18, 315.
- Okay, G., Leroy, P., Ghorbani, A., Cosenza, P., Camerlynck, C., Cabrera, J., et al. (2014). Spectral induced polarization of clay-sand mixtures: Experiments and modeling. *Geophysics* 79 (6), E353–E375. doi:10.1190/geo2013-0347.1
- Oldenburg, D. W., and Li, Y. (1994). Inversion of induced polarization data. *Geophysics* 59 (9), 1327–1341. doi:10.1190/1.1443692
- Papalexioiu, S. M., and Montanari, A. (2019). Global and regional increase of precipitation extremes under global warming. *Water Resour. Res.* 55 (6), 4901–4914. doi:10.1029/2018wr024067
- Parasnis, D. S. (2012). *Principles of applied geophysics*. Springer Science and Business Media.
- Pelton, W. H., Ward, S., Hallof, P., Sill, W., and Nelson, P. H. (1978). Mineral discrimination and removal of inductive coupling with multifrequency ip. *Geophysics* 43 (3), 588–609. doi:10.1190/1.1440839
- Perrone, A., Lapenna, V., and Piscitelli, S. (2014). Electrical resistivity tomography technique for landslide investigation: A review. *Earth-Science Rev.* 135, 65–82. doi:10.1016/j.earscirev.2014.04.002
- Revil, A., and Florsch, N. (2010). Determination of permeability from spectral induced polarization in granular media. *Geophys. J. Int.* 181 (3), 1480–1498. doi:10.1111/j.1365-246x.2010.04573.x
- Revil, A. (2012). Spectral induced polarization of shaly sands: Influence of the electrical double layer. *Water Resour. Res.* 48 (2). doi:10.1029/2011wr011260
- Revil, A., Kessouri, P., and Torres-Verdin, C. (2014). Electrical conductivity, induced polarization, and permeability of the fontainebleau sandstone. *Geophysics* 79 (5), D301–D318. doi:10.1190/geo2014-0036.1
- Revil, A., Florsch, N., and Mao, D. (2015). Induced polarization response of porous media with metallic particles—part 1: A theory for disseminated semiconductors. *Geophysics* 80 (5), D525–D538. doi:10.1190/geo2014-0577.1
- Revil, A., Coperey, A., Shao, Z., Florsch, N., Fabricius, I. L., Deng, Y., et al. (2017). Complex conductivity of soils. *Water Resour. Res.* 53 (8), 7121–7147. doi:10.1002/2017wr020655
- Revil, A., Ahmed, A. S., Coperey, A., Ravanel, L., Sharma, R., and Panwar, N. (2020). Induced polarization as a tool to characterize shallow landslides. *J. Hydrology* 589, 125369. doi:10.1016/j.jhydrol.2020.125369
- Rogers, N. W., and Selby, M. J. (1980). Mechanisms of shallow translational landsliding during summer rainstorms: North Island, New Zealand. *Geogr. Ann. Ser. A Phys. Geogr.* 62, 11–21. doi:10.2307/520448
- Rögl, F. (1997). “Palaeogeographic considerations for mediterranean and paratethys seaways (oligocene to miocene),” in *Annalen des Naturhistorischen Museums in Wien. Serie A für Mineralogie und Petrographie, Geologie und Paläontologie, Anthropologie und Prähistorie*, 279–310.
- Rücker, C., Günther, T., and Wagner, F. M. (2017). pygimli: An open-source library for modelling and inversion in geophysics. *Comput. Geosciences* 109, 106–123. doi:10.1016/j.cageo.2017.07.011
- Rupp, C., Linner, M., and Mandl, W. (2011). *Erläuterungen zur geologischen karte von oberösterreich*. Vienna: Verlag der Geologischen Bundesanstalt.
- Samyn, K., Travalletti, J., Bitri, A., Grandjean, G., and Malet, J.-P. (2012). Characterization of a landslide geometry using 3d seismic refraction traveltimes

- tomography: The la valette land- slide case history. *J. Appl. Geophys.* 86, 120–132. doi:10.1016/j.jappgeo.2012.07.014
- Schaap, M. G., Leij, F. J., and Van Genuchten, M. T. (2001). Rosetta: A computer program for estimating soil hydraulic parameters with hierarchical pedotransfer functions. *J. hydrology* 251 (3–4), 163–176. doi:10.1016/s0022-1694(01)00466-8
- Schnyder, J., Ruffell, A., Deconinck, J.-F., and Baudin, F. (2006). Conjunctive use of spectral gamma-ray logs and clay mineralogy in defining late jurassic–early cretaceous palaeoclimate change (dorset, u.k.). *Palaeogeogr. Palaeoclimatol. Palaeoecol.* 229 (4), 303–320. doi:10.1016/j.palaeo.2005.06.027
- Searchinger, T. D., Wirsenius, S., Beringer, T., and Dumas, P. (2018). Assessing the efficiency of changes in land use for mitigating climate change. *Nature* 564 (7735), 249–253. doi:10.1038/s41586-018-0757-z
- Sidle, R. C., Greco, R., and Bogaard, T. (2019). Overview of landslide hydrology. *Water* 11, 148. doi:10.3390/w11010148
- Slater, L., Barrash, W., Montrey, J., and Binley, A. (2014). Electrical-hydraulic relationships observed for unconsolidated sediments in the presence of a cobble framework. *Water Resour. Res.* 50 (7), 5721–5742. doi:10.1002/2013wr014631
- Slater, L. D., and Reeve, A. (2002). Investigating peatland stratigraphy and hydrogeology using integrated electrical geophysics. *Geophysics* 67 (2), 365–378. doi:10.1190/1.1468597
- Slater, L., and Glaser, D. (2003). Controls on induced polarization in sandy unconsolidated sediments and application to aquifer characterization. *Geophysics* 68 (5), 1547–1558. doi:10.1190/1.1620628
- Slater, L., and Lesmes, D. P. (2002). Electrical-hydraulic relationships observed for unconsolidated sediments. *Water Resour. Res.* 38 (10), 31–1–31–13. doi:10.1029/2001wr001075
- Spies, B. (1996). Electrical and electromagnetic borehole measurements: A review. *Surv. Geophys.* 17 (4), 517–556. doi:10.1007/bf01901643
- Supper, R., Ottowitz, D., Jochum, B., Kim, J.-H., Römer, A., Baron, I., et al. (2014). Geoelectrical monitoring: An innovative method to supplement landslide surveillance and early warning. *Near Surf. Geophys.* 12 (1), 133–150. doi:10.3997/1873-0604.2013060
- Tabari, H. (2020). Climate change impact on flood and extreme precipitation increases with water availability. *Sci. Rep.* 10 (1), 1–10. doi:10.1038/s41598-020-70816-2
- Tarasov, A., and Titov, K. (2007). Relaxation time distribution from time domain induced polarization measurements. *Geophys. J. Int.* 170 (1), 31–43. doi:10.1111/j.1365-246x.2007.03376.x
- Twarakavi, N. K., Simunek, J., and Schaap, M. (2009). Development of pedotransfer functions for estimation of soil hydraulic parameters using support vector machines. *Soil Sci. Soc. Am. J.* 73 (5), 1443–1452. doi:10.2136/sssaj2008.0021
- Uhlemann, S., Hagedorn, S., Dashwood, B., Maurer, H., Gunn, D., Dijkstra, T., et al. (2016). Landslide characterization using p-and s-wave seismic refraction tomography—The importance of elastic moduli. *J. Appl. Geophys.* 134, 64–76. doi:10.1016/j.jappgeo.2016.08.014
- Van Genuchten, M. T. (1980). A closed-form equation for predicting the hydraulic conductivity of unsaturated soils. *Soil Sci. Soc. Am. J.* 44 (5), 892–898. doi:10.2136/sssaj1980.03615995004400050002x
- Van Looy, K., Bouma, J., Herbst, M., Koestel, J., Minasny, B., Mishra, U., et al. (2017). Pedotransfer functions in earth system science: Challenges and perspectives. *Rev. Geophys.* 55 (4), 1199–1256. doi:10.1002/2017rg000581
- Ward, S. H., and Hohmann, G. W. (1988). “Electromagnetic theory for geophysical applications,” in *Electromagnetic methods in applied geophysics: Volume 1, theory* (Society of Exploration Geophysicists), 130–311. doi:10.1190/1.9781560802631.ch4
- Ward, S. H. (1990). Resistivity and induced polarization methods. *Geotechnical Environ. Ment. Geophys.* 1, 147–189. doi:10.1190/1.9781560802785.ch6
- Watlet, A., Kaufmann, O., Triantafyllou, A., Poulain, A., Chambers, J. E., Meldrum, P. I., et al. (2018). Imaging groundwater infiltration dynamics in the karst vadose zone with long-term ERT monitoring. *Hydrol. Earth Syst. Sci.* 22 (2), 1563–1592. doi:10.5194/hess-22-1563-2018
- Waxman, M. H., and Smits, L. J. M. (1968). Electrical conductivities in oil-bearing shaly sands. *Soc. Petroleum Eng. J.* 8 (02), 107–122. doi:10.2118/1863-a
- Weiskopf, S. R., Rubenstein, M. A., Crozier, L. G., Gaichas, S., Griffis, R., Halofsky, J. E., et al. (2020). Climate change effects on biodiversity, ecosystems, ecosystem services, and natural resource management in the United States. *Sci. Total Environ.* 733, 137782. doi:10.1016/j.scitotenv.2020.137782
- Weller, A., Nordsiek, S., and Debschütz, W. (2010). Estimating permeability of sandstone samples by nuclear magnetic resonance and spectral-induced polarization. *Geophysics* 75 (6), E215–E226. doi:10.1190/1.3507304
- Weller, A., Slater, L., Binley, A., Nordsiek, S., and Xu, S. (2015). Permeability prediction based on induced polarization: Insights from measurements on sandstone and unconsolidated samples spanning a wide permeability range. *Geophysics* 80 (2), D161–D173. doi:10.1190/geo2014-0368.1
- Weller, A., and Slater, L. (2019). Permeability estimation from induced polarization: An evaluation of geophysical length scales using an effective hydraulic radius concept. *Near Surf. Geophys.* 17 (6), 581–594. doi:10.1002/nsg.12071
- Whiteley, J. S., Watlet, A., Kendall, J. M., and Chambers, J. E. (2021). Brief communication: The role of geophysical imaging in local landslide early warning systems. *Nat. Hazards Earth Syst. Sci.* 21, 3863–3871. doi:10.5194/nhess-21-3863-2021
- Zhang, Y., and Schaap, M. G. (2019). Estimation of saturated hydraulic conductivity with pedotransfer functions: A review. *J. Hydrology* 575, 1011–1030. doi:10.1016/j.jhydrol.2019.05.058
- Zhang, Y., and Schaap, M. G. (2017). Weighted recalibration of the rosetta pedotransfer model with improved estimates of hydraulic parameter distributions and summary statistics (rosetta3). *J. Hydrology* 547, 39–53. doi:10.1016/j.jhydrol.2017.01.004

APPENDIX

Additionally to the saturated hydraulic conductivity K_s the Rosetta PTF (Schaap et al., 2001; Zhang and Schaap, 2017) predicts the parameters of the van Genuchten water retention function (Van Genuchten, 1980):

$$\theta(\psi) = \theta_r + \frac{\theta_s - \theta_r}{[1 + (\alpha|\psi|)^n]^{1-1/n}} \quad (A1)$$

in which $\theta_r(\psi)$ is the water retention curve in $\text{cm}^3\text{cm}^{-3}$ as a function of soil water pressure ψ , θ_r and θ_s are the residual and saturated water contents in $\text{cm}^3\text{cm}^{-3}$ and n (dimensionless) and α ($1/\text{cm}$) are curve shape parameters. Figure A1 shows the predicted van Genuchten parameters for the profile WD13 and the soil texture that was used as input for Rosetta.

